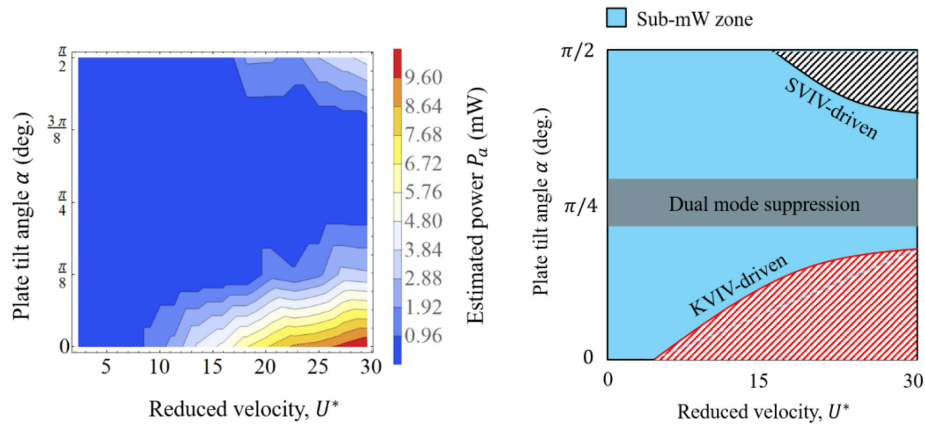


Graphical Abstract

Vortex-induced Vibration of an Angled Cruciform for Energy Harvesting

Ahmad Adzlan, Mohamed Sukri Mat Ali, Sheikh Ahmad Zaki



Highlights

Vortex-induced Vibration of an Angled Cruciform for Energy Harvesting

Ahmad Adzlan,Mohamed Sukri Mat Ali,Sheikh Ahmad Zaki

- Three main energy harvesting regimes were identified, based on the cruciform angle
- The streamwise-vortex induced vibration regime produces power in the order of 1 mW
- Power output is below 1 mW between angles 67.5° and 22.5°
- Power output can achieve up to 10 mW, as the angle is brought closer to 0° .

Vortex-induced Vibration of an Angled Cruciform for Energy Harvesting

Ahmad Adzlan^{a,b,*}, Mohamed Sukri Mat Ali^a and Sheikh Ahmad Zaki^a

^aMalaysia-Japan International Institute of Technology, Universiti Teknologi Malaysia, 54200 Kuala Lumpur, Malaysia

^bFaculty of Engineering, Universiti Malaysia Sarawak, 94300 Kota Samarahan, Sarawak, Malaysia

ARTICLE INFO

Keywords:

Vortex-induced vibration
Vibration energy harvester
CFD simulation
Streamwise vorticity
Ensemble empirical mode decomposition (EEMD)
Hilbert transform

ABSTRACT

We investigated the displacement and lift time series of a circular cylinder - strip plate cruciform system for energy harvesting in the Reynolds number range $1.1 \times 10^3 \leq Re \leq 14.6 \times 10^3$, numerically using the open source C++ library: OpenFOAM. The Karman vortex-induced vibration (KVIV) regime was identified between reduced velocity, U^* , 2.3 and 13.6, while the streamwise vortex-induced vibration (SVIV) regime was identified between $18.2 \leq U^* \leq 29.5$. We analysed the cylinder displacement and lift time series using the Hilbert-Huang transform (HHT). Within this range of U^* , Karman vortex shedding contributes nearly as much as streamwise vortex shedding to the root-mean-square amplitude of total lift, while between $25.0 \leq U^* \leq 29.5$, the Karman component contribution is on average twice that of the streamwise component. These findings hint at the possibility to improve the power output of the harvester by a factor of two between $18.2 \leq U^* \leq 22.7$ and by a factor of three between $25.0 \leq U^* \leq 29.5$, if we can unite the contribution to the root-mean-square amplitude of the total lift under a single vibration-driving mechanism: the shedding of streamwise vortex.

1. Introduction

Streamwise vortex-induced vibration (SVIV) is a type of vortex-induced vibration (VIV) driven by vortical structures whose vorticity vector points in the direction of the free stream. In recent decades, there have been efforts to exploit the SVIV phenomenon from cruciform structures for energy harvesting, an example of which is given in Fig. The literature on this subject can be broadly categorised into two groups: how the mechanical properties of the oscillator (e.g., mass ratio, damping, etc.) affects the amplitude/frequency response of SVIV (Koide et al., 2009, 2013; Nguyen et al., 2012) and how the minutiae of the flow field affect the force driving the vibration of the cylinder, i.e. the fluid mechanical aspect of the system (Deng et al., 2007; Koide et al., 2017; Zhao and Lu, 2018).

In the first focus area, researchers studied some permutation of the following method to convert the vibration into electrical power. The method consists of a coil and magnet. The coil, which moves with the vibrating cylinder, creates relative motion against the magnet, which is placed in the hollow of the coil (Koide et al., 2009). While investigating the system at a Reynolds number in the order of $Re \sim O(10^4)$, Koide et al. (2009) showed that increased damping due to energy harvesting reduces the maximum vibration amplitude close to a factor of 4. Amplitude reduction due to increased total damping was also mentioned in Bernitsas et al. (2008); Bernitsas and Raghavan (2008); Bernitsas et al. (2009). Further investigation in Nguyen et al. (2012) revealed that damping not only affects the amplitude response of

*Corresponding author

 aafkhairi@graduate.utm.my (A. Adzlan); sukri.kl@utm.my (M.S.M. Ali); sheikh.kl@utm.my (S.A. Zaki)
ORCID(s): 0000-0003-0290-3185 (A. Adzlan); 0000-0001-6411-9965 (S.A. Zaki)

the cylinder but also narrows the synchronisation region between vortex shedding and cylinder vibration. Moreover, Nguyen et al. (2012) demonstrated a strong coupling between mass ratio and damping in determining both the width of the synchronisation region and the maximum amplitude response of the cylinder.

In the second focus area, investigators turned their attention to the details of the flow where streamwise vortex shedding occurs. One such study carefully shot motion pictures of the dye-injected flow (Koide et al., 2017) at Reynolds number in the order of $Re \sim O(10^3)$. A lower Reynolds number (Re) reduces the amount of turbulence in the flow, allowing a clearer shot of the vortex structures. Their study also highlights the higher level of turbulence produced by the circular cylinder-strip plate cruciform in contrast to the twin circular cylinder cruciform, which diminishes the periodicity of vortex shedding. Although visually enlightening, this and other more qualitative studies contribute little towards improving our understanding of the relationship between vortex shedding and the resulting lift. Deng et al. (2007) demonstrated a way to overcome such a shortcoming.

In their study, Deng et al. (2007) examined the flow field of a twin circular cylinder cruciform using computational fluid dynamics (CFD). Their domain stretches $28D$ in the streamwise direction, $16D$ in the transverse direction and $12D$ in the spanwise direction. They studied an Re range yet another order of magnitude smaller than that studied by Koide et al. (2017), possibly to get an even clearer visualisation of the vortical structures with less turbulence, and to ease computational requisites. At a fixed $Re = 150$, streamwise vortices form even at a gap ratio of 2. This result differs quite strikingly from Koide et al. (2006, 2007), conducted at an Re twice the order of magnitude of Deng et al. (2007), an indication that the minimum gap ratio needed for the onset of streamwise varies with respect to Re .

They also observed that when the gap ratio G , which they denote as L/D in their paper, increases from 3 to 4, the maximum amplitude of the lift coefficient increases by almost threefold. This can be attributed quite easily to the current vortex pair shed by the upstream cylinder. The downstream cylinder immediately disturbs the pair shed from the upstream cylinder when $G = 3$. The lift coefficient increases by about a factor of 3 when this immediate disturbance diminishes at $G = 4$. The visualisation of three-dimensional (3D) vorticity isocontours enables us to quickly establish this link vis-à-vis the lift coefficient signal. The authors use of CFD made this possible.

A similar study in the order of magnitude $Re \sim O(10^2)$ by Zhao and Lu (2018) particularly highlighted the immense utility of CFD as a tool to research SVIV or flow around a cruciform in general. They computed the sectional lift coefficient along the upstream cylinder, and the time history of this sectional lift coefficient revealed two different modes of vortex shedding, namely, parallel and K-shaped. They also paid attention to the local flow patterns that vary along the length of the upstream cylinder such as the trailing vortex flow, necklace vortex flow and flow in the small gap (denoted as SG flow). The discontinuities in the phase angle of the sectional lift coefficient along the upstream cylinder seems to suggest the inadequateness of attributing the lift coefficient to streamwise vortex shedding alone, particularly when Karman vortex streamlines were also observed some distance away from the junction of the cruciform. Shirakashi

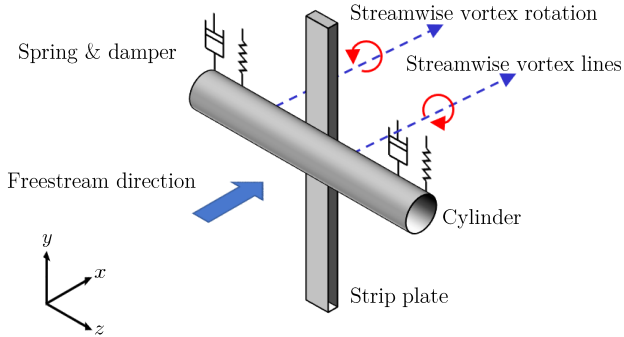


Figure 1: Schematic of the base configuration of the oscillator system used in this study, i.e. the pure cruciform. In this configuration, the axis of the cylinder and the strip plate are perpendicular to each other.

et al. (1989) also made a similar observation in their experimental work. This leads us to hypothesise that the lift signal is more appropriately viewed as the streamwise-Karman vortex-induced composite lift signal. However, we could not find studies that took this viewpoint and worked out its implication on power generation in their investigation of SVIV.

The objectives of this study are thus threefold: (1) to take a closer look at the amplitude and frequency response of a circular cylinder-strip plate cruciform, especially in reduced velocity (U^*) ranges where the transition from KVIV to SVIV occurs, (2) to demonstrate the compositeness of the lift signal of an SVIV system and establish the difference between the lift signal characteristics in the KVIV and SVIV regime and (3) to shed light on how the contribution from the Karman and streamwise components of lift changes as we increase U^* after the onset of SVIV and predict how much improvement in the power generation can be anticipated if we are able to unify the lift amplitude contributions due to Karman and streamwise vortex shedding. Here, $U^* = U/f_n D$, with U , f_n and D being the freestream velocity, natural frequency of the system and the diameter of the circular cylinder respectively. The following §2 details the methodology we employ to conduct this study. We present and discuss our results in. We describe our conclusions in §8.

2. Methodology

2.1. Problem geometry

This study bases itself on the work done by Maruai et al. (2017), Maruai et al. (2018), and Koide et al. (2013). In these works, the investigators conducted both experimental and computational investigations of passive control of FSI of cylinders using a strip plate located at the cylinder downstream. Here, the term “strip plate” is used as a shorthand for the long, rectangular plate used to control the vibration of the cylinder – since the plate resembles a strip due to its large aspect ratio. These studies demonstrated the feasibility of energy harvesting using the oscillator system described, in the Reynolds number range $3.6 \times 10^3 < Re < 12.5 \times 10^3$. Following this observation, we performed our numerical investigations within a similar Re range, albeit slightly widened, to check for variations in the cylinder response in as

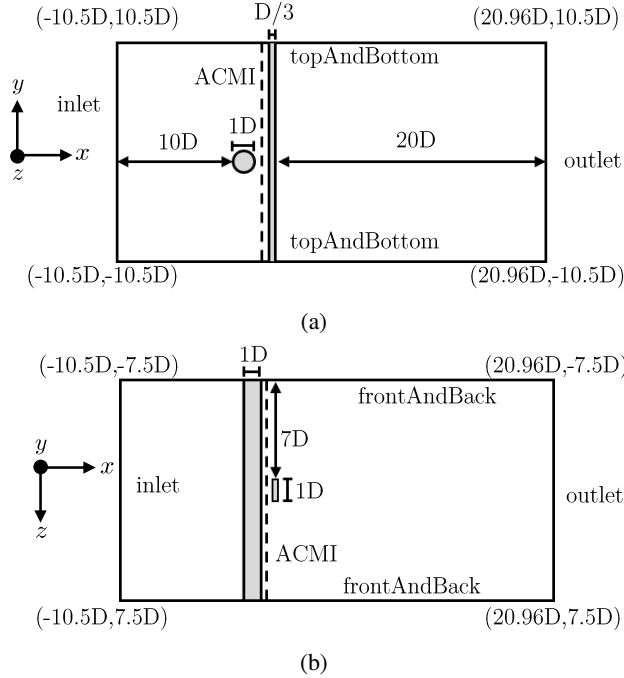


Figure 2: Figure 2a shows the cross-sectional layout of the computational domain, along with key dimensions, when viewed from the side. Figure 2b visualises the cross-section of the computational domain as viewed from the top. The arbitrarily coupled mesh interface (ACMI) used to connect the domain containing the cylinder with the domain containing the strip plate is placed halfway through the gap, i.e. $0.08D$ downstream the cylinder.

wide an Re range as possible, computational resources permitting.

Our oscillator system derives its geometry from the works of Nguyen et al. (2012), Koide et al. (2013), and Koide et al. (2017). The basic layout of our oscillator system is the pure cruciform: an arrangement where the circular cylinder and the strip plate located downstream have their axes perpendicular to each other. We fixed the gap between the cylinder and the strip plate, G , to 0.16. This value of G was chosen because the cylinder response most suitable for energy harvesting is sustained over the largest range of reduced velocity U^* when $G = 0.16$ (Koide et al., 2013).

Figure 2a visualises our computational domain from its side. We chose these dimensions based on analogous works such as Maruai et al. (2017) and Maruai et al. (2018) which had produced results that agree well with experiments of their own and with Kawabata et al. (2013). The streamwise coordinates of this domain extends from $-10.5D$ to $10.5D$, and the lateral coordinates from $-10.5D$ to $10.5D$. The coordinate origin $(0, 0, 0)$, is at the centre of the cylinder and the strip plate is $D/3$ thick.

In Fig. 2b, the circular cylinder extends from $z/D = 7.5$ to $z/D = -7.5$, giving the computational domain an overall spanwise length of $15D$. The computational domain of a similar study by Deng et al. (2007) has a length of $12D$, upon which the dimension of our domain is based upon. The extra $1.5D$ of spanwise length on either side of our domain is allocated to ensure the full expression of the three-dimensionality of flow structures that appear during the

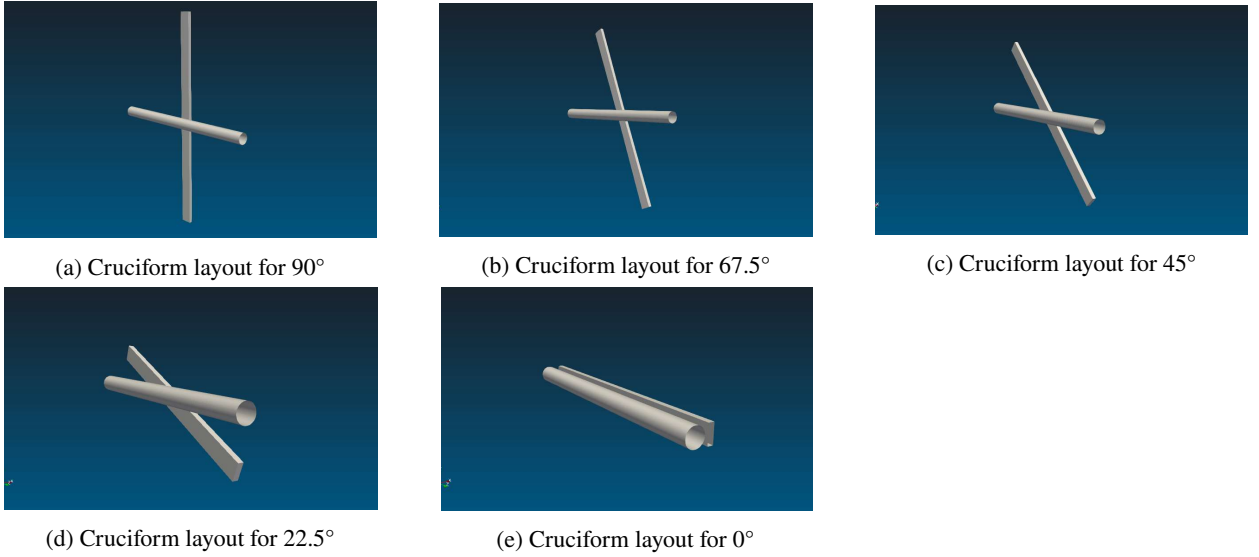


Figure 3: Variation of cruciforms studied in this work. We vary the cruciform angle from the case of a pure cruciform (90°) to the case of cylinder - plate in tandem (0°), in increments of 22.5° .

course of our numerical study.

We then produce variants of the pure cruciform configuration by rotating the strip plate from 90° to 0° in 22.5° increments. In total, we constructed five different cruciforms shown in Fig. 3. The dimensions of the computational domain remain fixed for all cruciforms, including the gap between the cylinder and the strip plate.

2.2. Numerical method

Our numerical study utilises OpenFOAM, an open-source computational fluid dynamics (CFD) platform written in C++. With OpenFOAM, we solved the 3D unsteady Reynolds averaged Navier-Stokes (3D URANS) equations that are the following.

$$\frac{\partial U_i}{\partial x_i} = 0, \quad (1)$$

$$\frac{\partial U_i}{\partial t} + U_j \frac{\partial U_i}{\partial x_j} = -\frac{1}{\rho} \frac{\partial P}{\partial x_i} + \frac{\partial}{\partial x_j} \left(2\nu S_{ij} - \overline{u'_j u'_i} \right). \quad (2)$$

The symbols U , x , t , ρ , P , ν , S , and u' denote the mean component of velocity, spatial component, time, density, pressure, kinematic viscosity, mean strain rate and the fluctuating component of velocity, respectively. Equation 3

gives the mean strain rate S_{ij} .

$$S_{ij} = \frac{1}{2} \left(\frac{\partial U_i}{\partial x_j} + \frac{\partial U_j}{\partial x_i} \right). \quad (3)$$

The turbulence model employed to approximate the Reynolds stress tensor is the Spalart-Allmaras turbulence model. Previous numerical studies on energy harvesting from FIM of circular cylinders have shown reasonable agreement with experiments in the literature through the use of this turbulence model, and thus becomes the basis for the implementation of the same turbulence model in our study (Ding et al., 2015a,b). The Boussinesq approximation relates the Reynolds stress tensor $\tau_{ij} = \overline{u'_j u'^i}$ to the mean velocity gradient, exemplified by Eq. 4.

$$\tau_{ij} = 2\nu_T S_{ij}, \quad (4)$$

where ν_T represents the kinetic eddy viscosity. This kinetic eddy viscosity is ultimately expressed as a function whose arguments consist of the molecular viscosity ν , and an intermediate variable \tilde{v} that is the solution of Eq. 5. Equation 5 incorporates empirically obtained constants to provide closure to the equations governing our numerical investigation. We list the empirical constants that make up Eq. 5 in Table 1.

$$\frac{\partial \tilde{v}}{\partial t} + U_j \frac{\partial \tilde{v}}{\partial x_j} = c_{b1} \tilde{S} \tilde{v} - c_{w1} f_w \left(\frac{\tilde{v}}{D} \right)^2 + \frac{1}{\sigma} \left\{ \frac{\partial}{\partial x_j} \left[(\nu + \tilde{\nu}) \frac{\partial \tilde{v}}{\partial x_j} \right] c_{b2} \frac{\partial \tilde{v}}{\partial x_i} \frac{\partial \tilde{v}}{\partial x_i} \right\} \quad (5)$$

Table 1
Empirical constants used in the Spalart-Allmaras turbulence model.

| Empirical constants | Value |
|---------------------|-------|
| c_{b1} | 0.01 |
| c_{b2} | 0.09 |
| c_{v1} | 0.01 |
| κ | 0.1 |
| σ | 0.162 |
| $c_{\omega3}$ | 0.178 |

We refer the interested reader to the original paper by Spalart and Allmaras (1992) and more recent applications of the turbulence model in Ding et al. (2019) and Sun et al. (2019). With the turbulence model properly defined, we are finally able to solve Eqs. 1 and 2 using the SIMPLE-stabilised PISO algorithm native to OpenFOAM, known as the PIMPLE algorithm.

2.3. Dynamic mesh motion

Cylinder motion in the computational domain due to FIV introduces distortion to the mesh immediately surrounding the cylinder. The simplest way to keep the mesh distortion in check, thus keeping mesh quality within an acceptable level, is by diffusing the amount of warping to the surrounding space. In practice, the surrounding space is the rest of the mesh nodes, and Eq. 6 governs the diffusion.

$$\nabla \cdot (\gamma \nabla u) = 0. \quad (6)$$

In Eq. 6, u and γ represents the mesh deformation velocity and displacement diffusion, respectively. In this work, we set the displacement to be diffused according to the inverse quadratic rule $\gamma = 1/l^2$. Here, l denotes the distance from the cell centre to the nearest cylinder edge. Then, we solve Eq. 6 using the GAMG algorithm and the Gauss-Seidel smoother. Solution of Eq. 6 returns an updated value of u , and this updated value of u is used to update the position of the mesh nodes according to Eq. 7. The PIMPLE solver resumes the solution of the 3D URANS equations after we update the mesh node positions.

$$x_{\text{new}} = x_{\text{old}} + u \Delta t \quad (7)$$

For most numerical studies of FSI, the mesh warp diffusion method governed by Eq. 6 serves as an adequate workaround to conserve mesh quality. However, this requires ample number of ambient mesh nodes acting as the receiving end of the diffusion algorithm. In our case, the small gap between the cylinder and strip plate ($G = 0.16$) pose a serious limitation to our ability to diffuse the amount of warp introduced by the displacement of the cylinder, since a small space means that we can only allocate a proportionate number of mesh nodes in said gap. Sole reliance on the warp diffusion algorithm will hamper our effort to preserve mesh quality as a high concentration of warp remains within the gap. To overcome this problem, we implement the arbitrarily coupled mesh interface (ACMI) halfway through the gap (see Fig. 2). This technique allows adjacent cells to slide over each other precisely at the $x = 0.13$ plane, ridding us of the requirement for mesh warp diffusion. In the literature, ACMI is also known as the generalised grid interface, or GGI (Zhang et al., 2018; Sun et al., 2019).

2.4. Open flow channel experiment

As part of the validation process for our numerical setup, we constructed a closed loop open flow channel, with a test section 100 mm wide, 200 mm high and 1500 mm long. The design of this open flow channel is heavily inspired

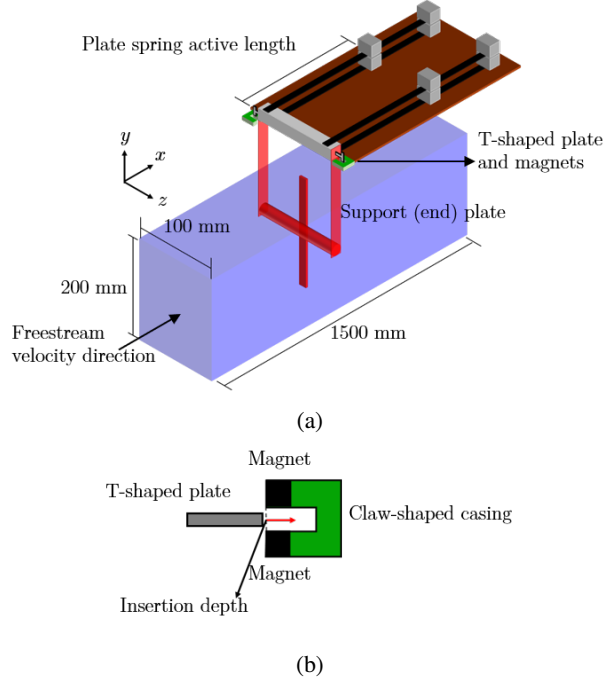


Figure 4: Our experimental system used to validate our numerical study. Figure 4a presents a 3D schematic of the open channel test section with a pure cruciform oscillator setup, while Fig. 4b shows a magnified schematic of the damping system.

by the water tunnel of Nguyen et al. (2012) and Koide et al. (2013). Considering the application of this research in the far future is in open flows such as natural drainage systems or the ocean - and not within pipes - prompts us to make this distinction.

We benchmark the open flow channel by setting up a pure cruciform oscillator (90°) experiment, whose data from similar studies are readily available in published works. Following this, we dimensioned the rig to follow the parameters used in Koide et al. (2013). A summary of our parameters and those used in Koide et al. (2013) are provided in Table 2. We tune the parameters governing the amplitude/frequency response of the oscillator using simple length-based mechanism as follows (see Fig. 4a). To tune the spring coefficient k , we simply adjust the active length of the twin spring plate. In practice, we obtained the calibration curve of the twin spring plate by performing a weight - displacement measurement (Sun et al., 2016) at several active lengths of the plate. Once the spring coefficient versus spring plate active length calibration curve is obtained, we can just adjust the length of the spring plate to achieve the desired value of k .

Tuning the total damping of the system and consequently the multiple expressions of damping such as the logarithmic damping δ , Scruton number Sc , or the damping coefficient is done by attaching, as shown in Fig. 4a, a T-shaped plate made from aluminium into a claw-shaped casing that houses neodymium magnets at its ends. As presented in Fig. 4b, the method we use to control the strength of the magnetic field exposed to the T-shaped plate is by fixing the

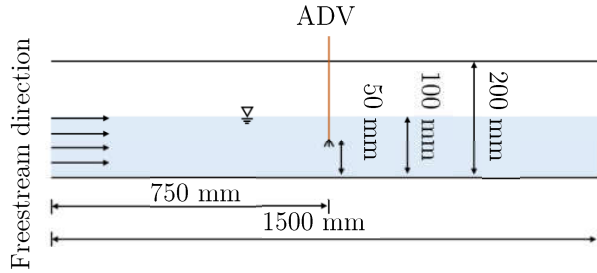


Figure 5: The side view of our test section. For a more valid benchmarking of our open channel flow with a similar system in Koide et al. (2013), we keep the water level to 100 mm.

insertion depth of the T-shaped plate into the casing. The magnetic field serves to dissipate the kinetic energy of the T-shaped plate that moves with the cylinder during FIM, providing system damping.

Table 2

Summary of experimental parameters in contrast to those used in the experimental work of Koide et al. (2013).

| | Current study | Koide et al. (2013) |
|--|---------------|---------------------|
| Cylinder diameter, D (m) | 0.01 | 0.01 |
| Cylinder length, l_{cylinder} (m) | 0.09 | 0.098 |
| Strip-plate width (m) | 0.01 | 0.01 |
| Strip-plate length (m) | 0.1 | 0.1 |
| Effective mass, $m_{\text{eff.}}$ (kg) | 0.162 | 0.174 |
| Logarithmic damping, δ | 0.178 | 0.24 |
| Scruton number, Sc | 9.94 | 7.74 |
| System natural frequency, f_n (Hz) | 4.42 | 4.4 to 4.79 |

A voltage controller regulates the power driving the 3.728 kW (5 hp) centrifugal pump. To set the freestream velocity in the open flow channel, we placed an acoustic Doppler velocimeter (ADV) sampling at in an empty test section, filled with plain tap water to a height of 100 mm, on the centreline of the channel, as pictured in Fig. 5. The height of 100 mm is also the water level we conduct our experiments in. We keep the water level at this height of 100 mm during all data collections to achieve a flow ambience analogous to our benchmark study of Koide et al. (2013), facilitating comparison between the two. Then, we sampled the velocity of the flow at different input voltages by the voltage controller, the final product being an input voltage V_{in} (V) versus centreline velocity U_{cent} calibration curve. This calibration curve allows us to set the freestream velocity of the open flow channel by specifying the input voltage to the pump. The finished product gave an operability range between 0.3 m/s and 1.1 m/s, which translates to $6.8 \leq U^* \leq 25.0$ for a circular cylinder of diameter 10 mm. The turbulence level ranges between 5% to 8% when the freestream velocity $U_{\infty} \geq 0.8$ m/s.

We measured the cylinder displacement y as a function of time by placing a visual marker on the support plate of the cylinder (see Fig. 4a) and capturing the motion of the marker using a video camera positioned perpendicular to the support plate. The motion of the marker is then analysed using *Tracker*: a motion analysis tool built on the

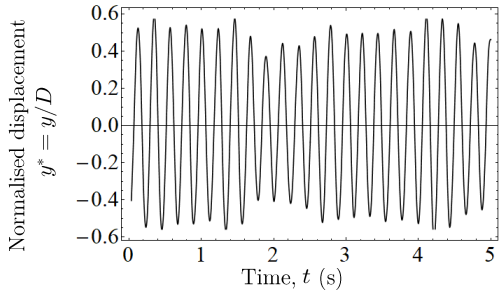


Figure 6: The normalised cylinder displacement measured as a function of time at $U^* = 22.7$. The experiment was repeated several times to estimate the uncertainty of the measured quantities y^* and f^* .

Open Source Physics Java framework (for recent implementation examples, see Wen et al. (2020) or Krishnendu and Ramakrishnan (2020)).

For the benchmarking, we chose the reduced velocity $U^* = 22.7$, as the cylinder at that U^* produces a large and stable displacement that simplifies on our part, the measurement and comparison process between our experimental system and Koide et al. (2013). A sample of the normalised displacement – $y^* = y/D$ – measured as a function of time is illustrated in Fig. 6. This time series allows us to also compute the normalised cylinder vibration frequency, $f^* = f_{\text{cyl}}/f_n$ (f_{cyl} being the vibration frequency of the cylinder). The y^* data presented in Fig. 6 returns $y^* = 0.33 \pm 0.03$ and $f^* = 1.03 \pm 0.04$, after computing the uncertainty from multiple experimental runs. In their work, Koide et al. (2013) obtained $y^* = 0.32$ and $f^* = 1.09$ at a similar U^* - values that are well within the measurement uncertainty of our experiment. This provides a basis for our reliance on results obtained from the experimental system later in the study.

3. Numerical setup validation

3.1. Grid independency study via Richardson extrapolation and grid convergence index

Like the first, the second method solves the governing equations on successively finer grids. However, instead of arguing that one obtains similar results on all the grids, the investigator checks whether the quantities of interest tend towards value, as one solves the governing equation on successively finer grid resolutions (Richardson and Gaunt, 1927; Stern et al., 2001). This method, of checking for convergence pays attention not only on the presumed converged value but also on the trend of convergence. Literature that employ this method impose a monotonic convergence condition (Stern et al., 2001; Mat Ali et al., 2011; Ali et al., 2012; Maruai et al., 2018) on their quantities of interest, adding an extra layer of confidence in the final form of their spatial discretisation.

Additionally, this method allows for a quantitative description of the degree of convergence through the grid convergence index (GCI). Let $f_1, f_2, f_3, \dots, f_k$ denote the quantity of interest obtained from several grids. A larger subscript indicates a coarser grid, thus, f_1 denotes the finest while f_k denotes the coarsest grid. Let the difference between

successive solutions be $\epsilon_{2,1}, \epsilon_{3,2}, \epsilon_{4,3}, \dots, \epsilon_{n,n-1}$, where $\epsilon_{2,1} = f_2 - f_1$, $\epsilon_{3,2} = f_3 - f_2$ and so on. Then, the GCI is defined as

$$\text{GCI}_{i+1,i} = F_s \frac{|\epsilon_{i+1,i}|}{f_i(r^p - 1)} \times 100\%, \quad (8)$$

where F_s , f_i and r^p denotes the safety factor ($= 1.25$), quantity of interest and the refinement ratio, r , between successive grids raised to the order of accuracy of the series of solution, p . We refer the reader to Stern et al. (2001); Langley Research Centre (2018) for a more detailed discussion on r^p .

We can estimate what the solution approaches as the grid size approaches zero by using the p^{th} method. Briefly, we compute the generalised Richardson extrapolation of the quantity of interest as follows.

$$f_{\text{RE}} = f_1 + \frac{f_1 - f_2}{r^p - 1}, \quad (9)$$

where f_{RE} is the Richardson extrapolation of the quantity of interest. Using f_{RE} to estimate the limit of the monotonically convergent series of f_i , we can determine the percentage difference of our solution on our finest grid from this limit as

$$E_i = \frac{f_i - f_{\text{RE}}}{f_{\text{RE}}} \times 100\%. \quad (10)$$

Table 3 summarises the result of our grid independency study for the SVIV reduced velocity of $U^* = 22.7$. We identified three quantities central to the investigation of fluid-structure phenomena, especially the flow-induced vibration of a circular cylinder. They are the vibration amplitude, vibration frequency and lift coefficient of the cylinder. We solve the governing equations on three grids which are numbered 1 for the finest, 2 for the medium and 3 for the coarsest, shown in Fig. 7. If we let v_i be the volume of the i^{th} cell in the grid and N be the total number of cells in the domain, then, the average cell size is

$$h = \frac{1}{N} \left[\sum_{i=1}^N v_i \right]^{1/3}, \quad (11)$$

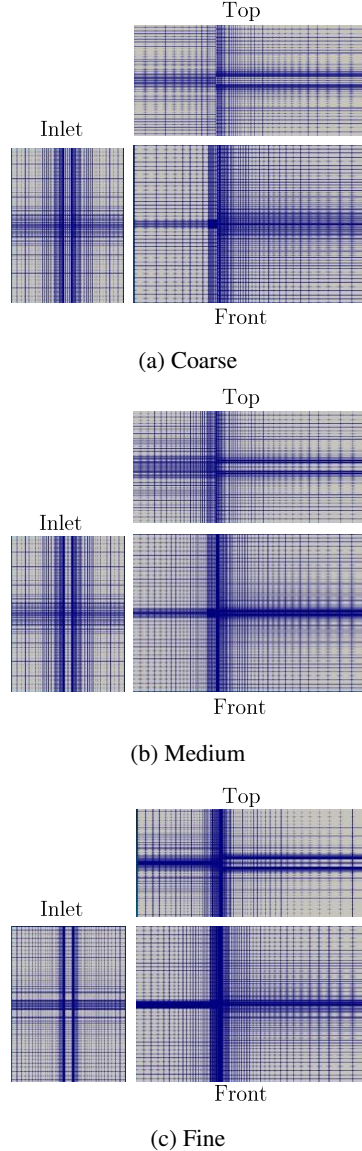


Figure 7: Three meshes used in the grid convergence study. Figures 7a, 7b and 7c show the coarse, medium and fine meshes viewed perpendicular to three main viewing positions: from the inlet, the top and the front, which is looking directly at the cylinder end.

and the normalised average cell size is hence

$$h/D = \frac{1}{ND} \left[\sum_{i=1}^N v_i \right]^{1/3}. \quad (12)$$

Both y_{RMS}^* and Cl_{RMS} starts at an initial value smaller than their Richardson extrapolations, f_{RE} , before approaching it as we decrease the average cell size, h . This similar trend can perhaps be attributed to the causal relationship between

the lift coefficient and vibration amplitude. The lift drives and sustains the vibration, hence a small lift produces a small vibration, and when the lift amplitude becomes higher, so too does the vibration amplitude. The vibration frequency, on the other hand, starts at a value larger than its f_{RE} before approaching f_{RE} .

The quantity Cl_{RMS} experiences the most significant drop in GCI as we refine the grid. The GCI is close to one-third (30.92%) as we refine the grid from coarse to medium with a refinement ratio of 1.376. The refinement ratio is calculated by dividing the number of cells in one grid with the next one down the refinement line. Following the grid numbering convention explained previously, dividing the number of cells in the fine grid (grid 1) with the number of cells in the medium grid (grid 2) gives us the refinement ratio from medium to fine, or $r_{2,1}$. Similarly, dividing the number of cells in the medium grid (grid 2) with the number of cells in the coarse grid (grid 3) gives us the refinement ratio from coarse to medium, or $r_{3,2}$. We can generalise this to i -number of grids as follows.

$$r_{i+1,i} = \frac{S_{\text{grid},i+1}}{S_{\text{grid},i}}, \quad (13)$$

where $S_{\text{grid},i}$ denotes the total number of cells in the i^{th} grid. The GCI of Cl_{RMS} drops further to 1.63% as the mesh is refined more with a refinement ratio of 1.304.

The GCI for y_{RMS}^* also drops by one order of magnitude as can be seen by comparing $GCI_{3,2}$ with $GCI_{2,1}$. Again, this similar trend of improvement points to the causal relationship between lift and displacement of the cylinder. The GCI for f^* , however, drops by approximately a factor of 6 instead of one order of magnitude, unlike the GCIs of y_{RMS}^* and Cl_{RMS} .

Table 3
Summary of grid independency study.

| Parameter/ metric | Cl_{RMS} | $y_{RMS}^* = y^*/D$ | $f^* = f_{cyl.}/f_n$ |
|---|------------|---------------------|----------------------|
| f_{RE} | 0.262 | 0.369 | 0.969 |
| f_1 | 0.2598 | 0.3687 | 0.9695 |
| f_2 | 0.2430 | 0.3588 | 0.9740 |
| f_3 | 0.0805 | 0.2374 | 1.0220 |
| $ \epsilon_{2,1} $ | 0.02 | 0.01 | 0.004 |
| $ \epsilon_{2,1} $ | 0.16 | 0.12 | 0.48 |
| $R = \epsilon_{2,1} / \epsilon_{2,1} $ | 0.10 | 0.08 | 0.094 |
| $GCI_{3,2}$ | 30.92 | 6.00 | 0.64 |
| $GCI_{3,2}$ | 1.63 | 0.52 | 0.10 |

We provide visual representations of the convergent Cl_{RMS} , y_{RMS}^* and f^* series in Figs. 8, 9 and 10. Note how the quantity of interest is very close to its Richardson extrapolation at the fine grid (grid 1) for all Cl_{RMS} , y_{RMS}^* and f^* . This implies that the fine grid already provides adequate spatial discretisation for the problem we are studying, and further refinements, while able to nudge our solutions even closer to the limit that is the Richardson extrapolation,

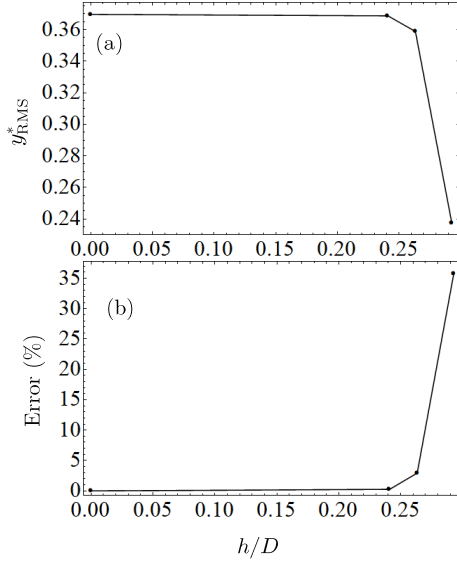


Figure 8: The convergence diagram for y_{RMS}^* . Figure 8a shows how y_{RMS}^* converges close to the Richardson extrapolation value while Fig. 8b shows how the error (difference between the value obtained from a particular mesh and the Richardson extrapolation) decreases with decreasing grid spacing.

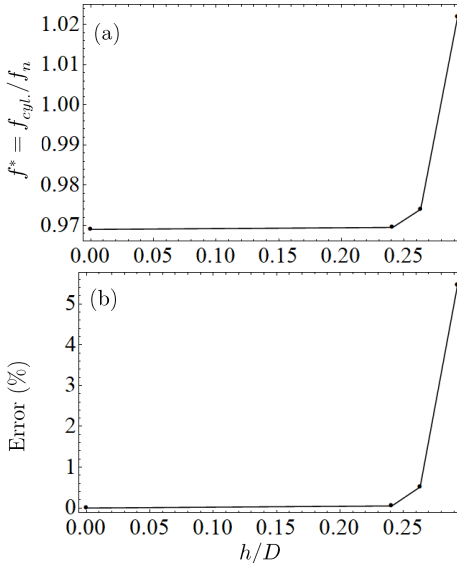


Figure 9: The convergence diagram for f^* . Figure 9a shows how f^* converges close to the Richardson extrapolation value while Fig. 9b shows how the error (difference between the value obtained from a particular mesh and the Richardson extrapolation) decreases with decreasing grid spacing.

may not be optimal in terms of usage of computational resources. Values of y_{RMS}^* and f^* at the fine grid already fall within experimental uncertainty as evidenced by our measurement in §2.4 and the work by Koide et al. (2013). Hence, all succeeding numerical data are gathered from the fine grid.

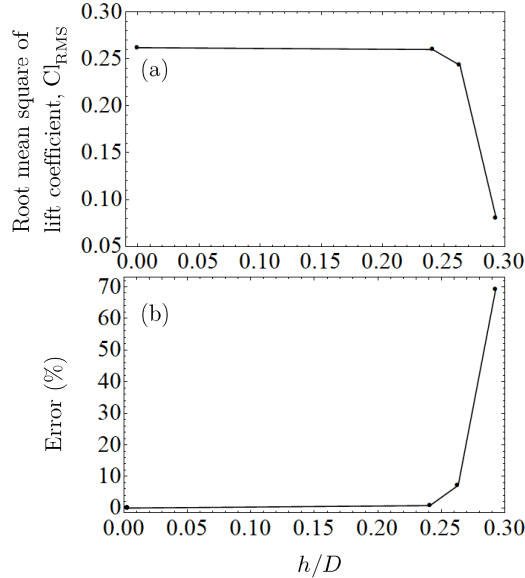


Figure 10: The convergence diagram for Cl_{RMS} . Figure 10a shows how Cl_{RMS} converges close to the Richardson extrapolation value while Fig. 10b shows how the error (difference between the value obtained from a particular mesh and the Richardson extrapolation) decreases with decreasing grid spacing.

4. Streamwise vortex-driven vibration

4.1. The amplitude and frequency response

The pure cruciform case, i.e. 90° , demonstrated a normalised root-mean-square amplitude of cylinder displacement, y_{RMS}^* that starts quite expectedly with a low amplitude at reduced velocities 2.3 and 4.5, before reaching a value close to $y_{RMS}^* = 0.1$ at $U^* = 6.8$, as presented in Fig. 11. Following the local maximum at $U^* = 6.8$, y_{RMS}^* tapers off to less than $y_{RMS}^* = 0.05$ between $9.1 \leq y_{RMS}^* \leq 13.6$. This whole y_{RMS}^* trend of hitting a local maximum before tapering off bears a striking resemblance to the amplitude response of an isolated circular cylinder in KVIV at mass ratios of order $O(10^1)$ (Feng, 1963; Khalak and Williamson, 1999). This resemblance can be seen as an indication that the vibration of a pure cruciform between $U^* \leq 15.9$ is driven primarily through the shedding cycle of Karman vortices.

Then at $U^* = 15.9$, y_{RMS}^* experiences a very weak increase followed by a sudden jump close to 0.4 at $U^* = 18.2$. This is followed by a slight decline at $U^* = 20.5$ and return to the previous level of y_{RMS}^* at $U^* = 22.7$. Past $U^* = 22.7$, we observe that y_{RMS}^* maintains a linear trend in its variation with respect to U^* . As $U^* = 18.2$ is well within the lower branch for a system in KVIV, it is quite unlikely for the vibration within $18.2 \leq U^* \leq 29.5$ to be the governed by the shedding of Karman vortices, leading previous investigators to attribute the vibration to the periodic shedding of streamwise vortical structures dominating the spatial region close to the cruciform juncture (Shirakashi et al., 1989; Hemsuwan et al., 2018b,a). Hence, we name this range of U^* the streamwise vortex-induced vibration regime.

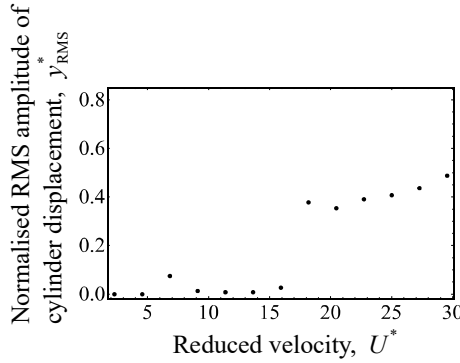


Figure 11: Evolution of the normalised root-mean-square amplitude of cylinder displacement y_{RMS}^* , with respect to reduced velocity U^* , in the streamwise vortex-driven vibration regime.

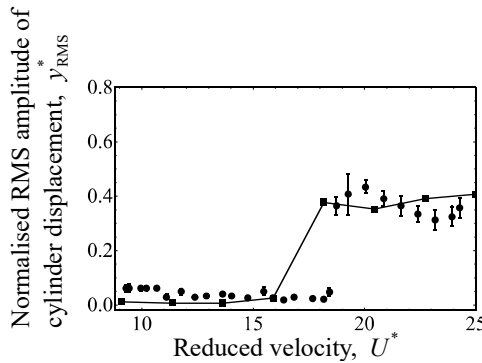


Figure 12: Comparison between the evolution of y_{RMS}^* with respect to U^* of a pure cruciform system from our numerical and experimental work. The filled square represents the numerical, while the filled circle represents the experimental results.

The experimental system consisting of the closed loop open flow channel and the pure cruciform oscillator rig in §2.4 is constructed not only for the purpose of validating the results of our pure cruciform numerical investigation, but also to corroborate in general, the sum total of our numerical setup. Admittedly, the best undertaking would be to perform equivalent experiment for each of the 90° , 67.5° , 45° , 22.5° and 0° configurations, but the scale of such an exercise and subsequent discussion of the results in our opinion, deserves its own treatment separate from the current study. The degree of agreement between the results of our numerical and experimental investigation of the pure cruciform establishes the validity of our numerical setup, which we assume to extend to the rest of the cruciforms. We think that this assumption is somewhat founded because all cruciforms are simulated under similar boundary conditions, mesh resolution and solver algorithm.

Our experiments collect time series data of cylinder displacement y , from which the normalised root-mean-square amplitude y_{RMS}^* is computed. Figure 12 compares both our numerical and experimental results of y_{RMS}^* . We observe that both results agree in terms of magnitude and trend of the amplitude response. However, the jump to SVIV occurs at a higher $U^* \approx 19$, translating to a delay of about 3 units of U^* . Our numerical and experimental results are also

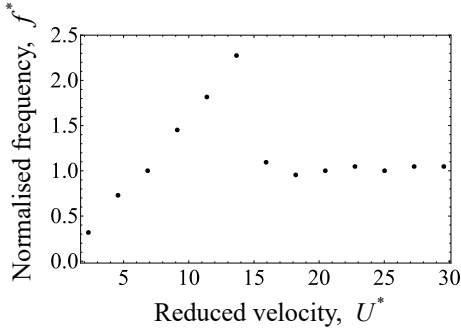


Figure 13: Evolution of the normalised cylinder displacement frequency, f^* , with respect to reduced velocity U^* , for the pure cruciform case.

able to capture the slight dip in y_{RMS}^* following the jump to SVIV, but the occurrence in our experiment is also delayed by about 3 units of U^* . This delay can perhaps be attributed to the fact that the raw y time series were measured in succession from the lowest attainable channel flow velocity 0.3 m/s to its highest 1.1 m/s within one experimental run. In contrast, our simulations always start with the cylinder at rest at its neutral position at $t_0 = 0$ s, with the freestream exactly set at the desired value 0.1 m/s, 0.2 m/s, ..., 1.3 m/s. Thus, the delays found in our experimental results may simply be the consequence of “flow memory”, a concept whose analogy can be found in undergraduate experiments to determine the critical Reynolds number transitioning from laminar to turbulent flow in smooth circular pipes. The “flow memory” is in our opinion none other than the manifestation of flow inertia due to fluid viscosity, where the flow has a natural tendency to retain its previous state before being overpowered by the flow momentum. This results in the delay found at the jump to SVIV and the local y_{RMS}^* minimum after the jump.

We show the evolution of the normalised cylinder vibration frequency f^* with respect to U^* in Fig. 13. Inspecting Fig. 13, we immediately notice two distinct evolutionary pattern for f^* with a sharp boundary at $U^* = 13.6$. Between $2.3 \leq U^* \leq 13.6$, the f^* trend follows closely the shedding frequency of Karman vortices from an isolated, fixed circular cylinder (Blevins, 1990). The Karman vortex shedding frequency is given as an empirical equation in Eq. 14.

$$f_{v,\text{Karman}} = 0.198 \left(1 - \frac{19.7}{\text{Re}} \right) DU \quad (14)$$

Here, $f_{v,\text{Karman}}$, D and U are the vortex shedding frequency, diameter of the isolated circular cylinder and U the freestream velocity respectively. We can easily see how $f_{v,\text{Karman}}$ is a linear function of U , and this is what gives rise to the linear pattern of f^* within $2.3 \leq U^* \leq 13.6$. Then, within $15.9 \leq U^* \leq 29.5$, f^* drops close to 1, indicating synchronisation between lift and cylinder vibration. We think this synchronisation is what gives rise to the bigger y^* , compared to $2.3 \leq U^* \leq 13.6$.

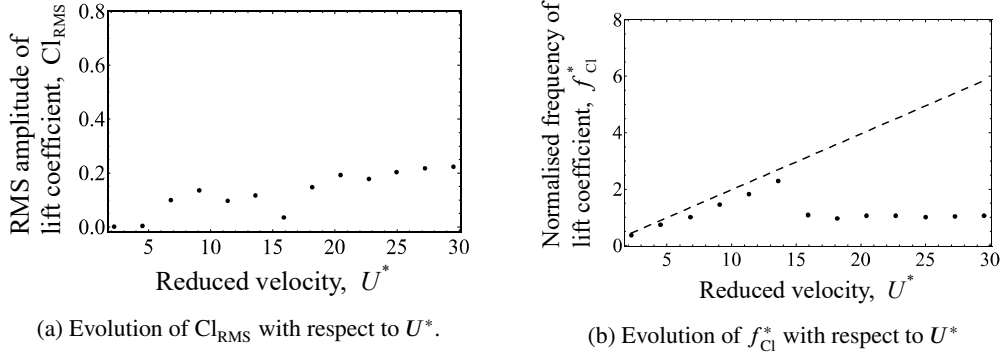


Figure 14: Evolution of the lift coefficient root-mean-square amplitude (Cl_{RMS}) and normalised frequency of lift coefficient (f_{Cl}^*), with respect to reduced velocity U^* , for the pure cruciform case. The dashed line in Fig. 14b visualises the shedding frequency of Karman vortex computed from Eq. 14.

Inspecting the evolution of root-mean-square amplitude of lift coefficient Cl_{RMS} and the normalised lift coefficient frequency f_{Cl}^* with respect to U^* in Fig. 14, provided more evidence supporting the assertion that $U^* = 15.9$ is a boundary between two vibration-driving mechanisms. In fact, the observation at 15.9 in Fig. 14a indicates that the SVIV regime is still in its infancy, due to the dip in Cl_{RMS} at that U^* , compared to $U^* = 13.6$. In Fig. 14b, we also draw a dashed line illustrating $f_v^* = f_{v,Karman}/D$, where $f_{v,Karman}$ is the shedding frequency of Karman vortices from a smooth isolated circular cylinder described in Eq. 14.

The trend found in f_{Cl}^* vs. U^* is very similar to that found in Fig. 13. We interpret this similarity as an indication of the symmetry of lift produced along the cylinder. Our reasoning stems from the findings of Zhao and Lu (2018), who revealed how lift is distributed along the upstream cylinder of a two-cylinder 90° cruciform. They did this by computing sectional lift coefficients along the upstream cylinder. This system produces a symmetric distribution of sectional lift coefficient, with $Z = 0$ being the plane of symmetry. An asymmetrical distribution of the sectional lift coefficient may produce a trend in y_{RMS}^* and f^* that is dissimilar to those found in Cl_{RMS} and f_{Cl}^* , due to the irregular moment acting on the cylinder.

4.2. Main vibration-driving vortical structure

Recall Figs. 11 and 13. Out of all thirteen variants of U^* studied in the pure cruciform case, seven within $15.9 \leq U^* \leq 29.5$ sustain high-amplitude vibrations with no foreseeable upper limit within our observation window. For a more complete understanding of the mechanism driving the vibration, we need to know what are the vortical structures dominating the flow and how they interact with each other.

Let us denote coordinates in our simulation domain in the following manner: $(X, Y, Z) = \left(\frac{x}{D}, \frac{y}{D}, \frac{z}{D}\right)$. We sampled the y -component velocity fluctuations on the $(X, Y) = (1.96, 0)$ line, along the span of the cylinder in $0.5D$ increments, i.e. at coordinates $(1.96, 0, 7.5), (1.96, 0, 7.0), \dots, (1.96, 0, -7.5)$. The distance $X = 1.96$ from the origin is equivalent

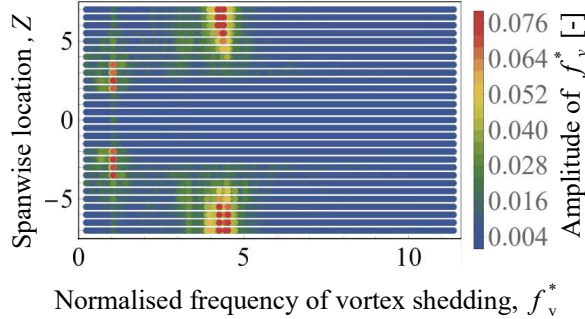


Figure 15: Distribution of normalised frequency of vortex shedding, along the span of the cylinder of the pure cruciform at $U^* = 22.7$.

to $1D$ downstream the trailing edge of the strip plate, and we chose this location as it is not too close to the cruciform that the vortical structures have not fully formed, and not too far, obfuscating meaningful observation of the structures.

The shedding of vortical structures leave their footprint on the flow field in the form of velocity fluctuations. Our choice of analysing the fluctuations of the y -component of velocity is made due to the fact that our oscillator is constrained to move only in the transverse direction. Then, we processed the velocity fluctuations with FFT to obtain the Fourier transform of the fluctuation signals at each spanwise location. The combined Fourier transforms are presented using a colour map in Fig. 15. In this figure, every point is a result of that FFT giving us a spatial understanding of the vortical structures present in the flow. The abscissa and ordinates denotes f^* and Z coordinates respectively, while the bar legend gives the amplitude of the FFT result.

Through inspection, we immediately notice two frequency bands with high amplitudes namely $f^* \approx 1$ and $f^* \approx 4.5$. The locations of these bands are between $3 \leq Z \leq 4.5$ for the former and $4.5 < Z \leq 7$ for the latter. Aided with this visualisation, we can give meaning to the x and z -components of vorticity visualised in Fig. 16. The slices in Fig. 16 visualise the distribution of the x (streamwise) and z (Karman) components of vorticity at the $X = 1.96$ plane. The plane is viewed from downstream (viewer standing at $X = 1.96$, looking towards the cruciform), and we present the vorticities in units of s^{-1} . Furthermore, the visualisations are made when the lift coefficient Cl is at a maximum (Cl_{max}).

Comparing Fig. 15 with Fig. 16 suggests that the $f^* \approx 1$ band is actually due to the shedding of streamwise vortex of a scale close to $1D$ while the $f^* \approx 4.5$ seems to be due to the shedding of Karman vortices. Contrary to the vortical structure commonly observed in studies of isolated circular cylinders (Deng et al., 2007; Kinaci et al., 2016; Duranay and Kinaci, 2020), in the pure cruciform case, two distinct vortical structures take shape in the flow, namely streamwise and Karman vortices. This is consistent with the findings in Koide et al. (2017) or Zhao and Lu (2018), where they observed a pair of streamwise vortices on a scale of $\approx 1D$ form in the vicinity of the cruciform juncture, and Karman vortices further away in the spanwise direction. Note that the vibration-driving streamwise vortices forming

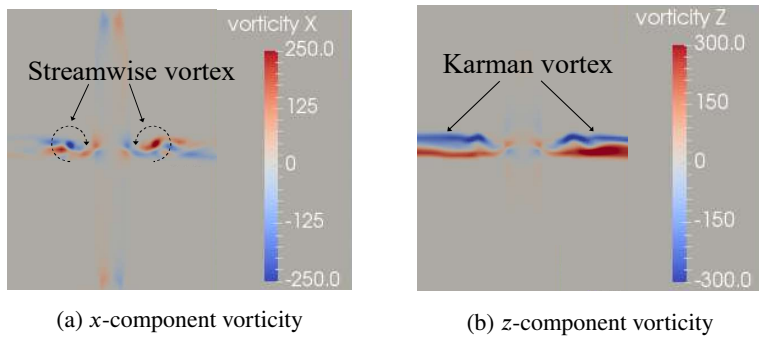


Figure 16: Dominant vortical structures at $U^* = 22.7$ observed in the pure cruciform case. The vorticity slices shown are the x and y -component vorticities at $x/D = 1.96D$ ($1D$ downstream the trailing edge of strip plate) plane, viewed orthogonal to that plane from downstream. The vorticities have a unit of s^{-1} .

close to the cruciform juncture exist in pairs: in Fig. 16a, we observe one rotate in the clockwise direction when $Z > 0$ and the other in the counter-clockwise direction when $Z < 0$. What results from this counter-rotating vortex pair is a downward thrust, propelling the cylinder upwards, and consistent with the fact that we visualised the vorticity fields when the Cl is at a maximum. We also observe the core of both streamwise vortices lie approximately on the same Y -plane, parallel to the axis of the cylinder.

4.3. Phase lag between Cl and y^*

In this study, we compute the phase lag $\theta_{y-\text{Cl}}$ by taking the Hilbert transform of both y^* and Cl signals, as Khalak and Williamson (1999) did in their VIV study of isolated circular cylinders. However, since Hilbert transform only produce physically meaningful results when used on monocomponent signals (Huang et al., 1998; Huang and Attoh-Okine, 2005; Huang, 2014), the signals first needs to be decomposed into components that satisfy the aforementioned condition, referred to in the literature as the intrinsic mode function (IMF). To achieve this, we implement the ensemble empirical mode decomposition (EEMD) (Wu and Huang, 2008).

The word “ensemble” in EEMD refers to the fact that it is an adaptation of the empirical mode decomposition (EMD) algorithm that takes the ensemble average of n -variants of the same IMF. The method outlined by the original authors of EEMD (Wu and Huang, 2008) to produce n -variants of the same IMF is by producing n white noise signals of equal length to the signal being decomposed, with an amplitude 10% to 20% the amplitude of the standard deviation of the original signal. Then, we add the n -number of white noise signals to the signal being decomposed, creating n -variants of the original signal. Each variant is then decomposed according to the following rule:

1. Connect all the signal maxima/minima with cubic splines, thus obtaining the signal envelope.
 2. Determine the local mean of the envelope for the span of the data.
 3. Compute the difference between the local mean of the envelope and the original data.
 4. Repeat steps 1 and 2 on the difference computed in 3 until we obtain our first IMF (IMF 1).

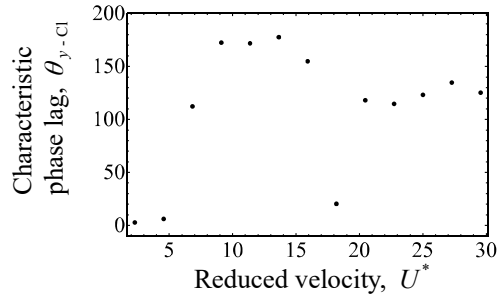


Figure 17: Phase lag θ_{y-Cl} (°) between Cl and y^* when 90° .

5. Subtract IMF 1 from the original signal and we are left with the remainder of the signal, upon which steps 1 to 4 are repeated, producing IMF 2, IMF 3 and so on until we are left with what is called the residual of the original signal, from which no more IMF can be extracted.

Since we constructed n -variants of the signal earlier, we effectively have, through the EMD algorithm described, derived n -variants of IMF 1, IMF 2 and so on. The ensemble part of EEMD now comes to play, when we averaged all n -variants of IMF 1, IMF 2, etc., giving us the ensemble version of each IMF. These are the IMFs that we use in our Hilbert transform. In this work, we produced 150 variants of the original signals using white noises 20% the amplitude of the standard deviation of the original signal.

Once the IMF components are retrieved, we compute the instantaneous phase of the IMFs C_1, C_2, \dots, C_i by constructing an analytical signal $z(t)$ from them in the following manner. First we compute the Hilbert transform of the IMF, H_i (see Eq. 15),

$$H_i(t) = \frac{1}{\pi} \text{PV} \int_{-\infty}^{\infty} \frac{C_i(\tau)}{t - \tau} d\tau, \quad (15)$$

where PV means the Cauchy principal value. Then, we construct $z(t)$ as shown in Eq. 16.

$$z(t) = C_i(t) + iH_i(t) = a(t) \cdot e^{i\theta(t)}. \quad (16)$$

The i in Eq. 16 represents the complex number. In the exponent form of $z(t)$, $a(t) = \sqrt{C_i^2(t) + H_i^2(t)}$ and $\theta(t) = \arctan(H_i/C_i)$ describes the instantaneous amplitude and phase of the IMF, respectively. The lift coefficient Cl and the cylinder displacement y each has their own instantaneous phases $\theta_{Cl}(t)$ and $\theta_y(t)$. The characteristic phase lag θ_{y-Cl}

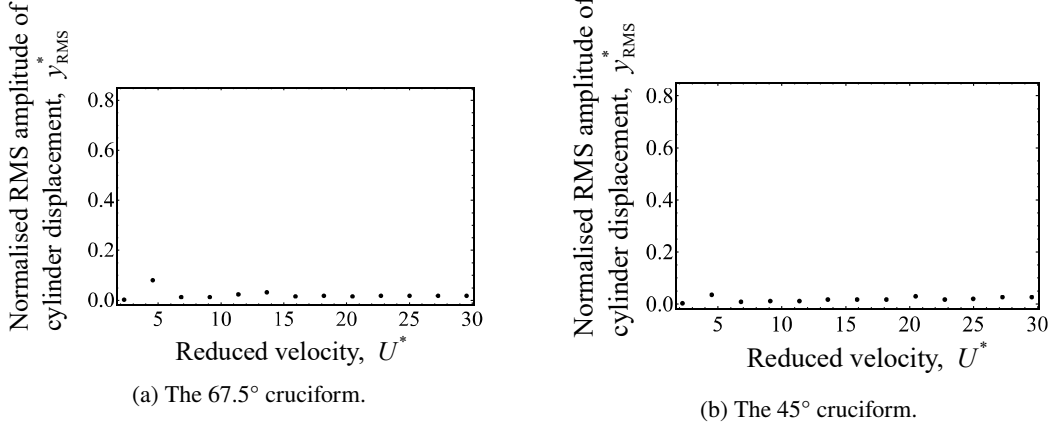


Figure 18: Evolution of the normalised root-mean-square amplitude of cylinder displacement y_{RMS}^* , with respect to reduced velocity U^* , for the 67.5° and 45° cruciform.

is thus defined such that

$$\theta_{y-\text{Cl}} = \frac{1}{T} \int_0^T [\theta_{\text{Cl}}(t) - \theta_y(t)] dt. \quad (17)$$

Out of C_i IMFs for each of y^* and Cl, we select the ones for computation of instantaneous phase according to the following rule. First, we choose the IMF component of y_{RMS}^* with the largest root-mean-square amplitude to represent the original y^* signal. Then, we choose the component of Cl with the highest correlation to the IMF component of y^* , to represent the Cl signal. The degree of correlation is determined by computing the cross-correlation between the two.

The characteristic phase angle $\theta_{y-\text{Cl}}$ defined in Eq. 17 is what we summarise against U^* in Fig. 17. Note that the $\theta_{y-\text{Cl}}$ pattern between $0 \leq U^* \leq 13.6$ resembles that which is found in isolated cylinder systems undergoing KVIV. We also observe that $\theta_{y-\text{Cl}}$ starts to drop when $U^* = 15.9$, supporting the view that a fundamental change in vibration-driving mechanism took place at that U^* , culminating in the emergence of the initial branch for SVIV at $U^* = 18.2$.

5. Transition to Karman vortex-driven vibration

5.1. The amplitude and frequency response

As we reduce the cruciform angle to 67.5° and 45° , we find that the SVIV branch observed in the pure cruciform case as $U^* \geq 15.9$ disappear, as one can inspect in Fig. 18. For the 45° cruciform, even y_{RMS}^* at the KVIV upper branch ($U^* = 4.5$) is lower than the corresponding values for both the 90° and 67.5° cruciforms.

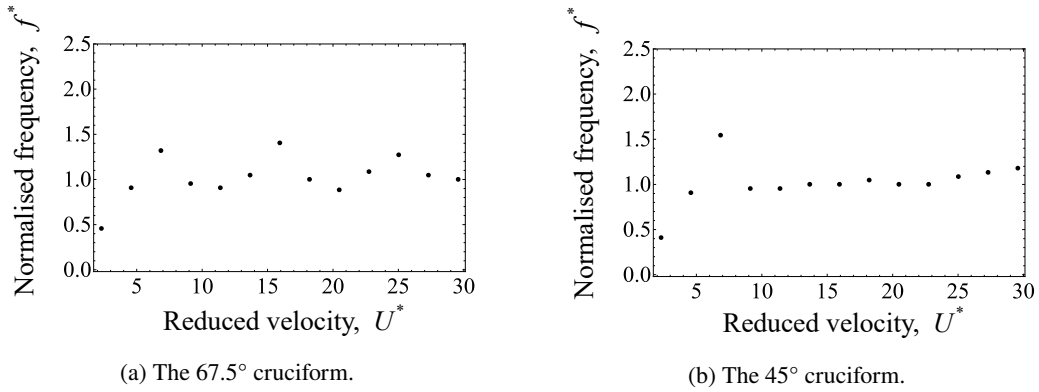


Figure 19: Evolution of the normalised cylinder displacement frequency, f^* , with respect to reduced velocity U^* , for the 67.5° and 45° cruciforms.

Another striking departure from the trend observed in the pure cruciform case, can be found in the evolution of f^* in Fig. 19. For the 67.5° cruciform in Fig. 19a, f^* seems to fluctuate with respect to U^* - suggesting asymmetry in the vortical structures regulating the vibration as discussed previously in §4.1. This fluctuation is however, not as pronounced in Fig. 21b, compared to Fig. 21a. We think this behaviour is due to the 45° cruciform being less similar to the 90° cruciform, in contrast to 67.5° . In other words, the 45° cruciform is less in transition from the response of the 90° cruciform and the flow around it is more evolved into its new configuration, unlike the 67.5° cruciform.

We summarised the root-mean-square lift coefficients Cl_{RMS} of the 67.5° and 45° cruciforms in Fig. 18. Here, we find that their evolution with respect to U^* in Figs. 20a and 20b approximates their corresponding y_{RMS}^* trend in Figs. 18a and 18b. As for the variation of f_{Cl}^* with respect to U^* , for both the 67.5° and 45° cruciforms, both exhibit outstanding similarity to $f_{v,Karman}$ of Eq. 14. This trait hints that vibrations resulting from the 67.5° and 45° cruciforms are primarily regulated by the shedding of Karman vortices.

The fact that the f_{Cl}^* trends observed in Figs. 21a and 21b do not lead to similar trends in the evolution of f^* in Figs. 19a and 19b leads us to believe there is something more fundamental at play in developing the f^* patterns we observed in Figs. 19. Hence we examined the vortical structures present in the flow surrounding the 67.5° and 45° cruciforms, and discuss our findings in §5.2.

5.2. Main vibration-driving vortical structure

As the first step, we computed the FFT of the y -component of velocity similar to what we did in Fig. 15 for both the 67.5° and 45° cruciforms. Our initial assessment of the $f_{v,Karman}^*$ distribution along the cylinder axis in Figs. 22a and 22b is that there is a strong representation of the Karman shedding frequency in both cases, which at $U^* = 22.7$ is $f_{v,Karman}^* = 4.49$. However, unlike Fig. 15, there is no frequency band close to 1 around the cruciform juncture.

Our first guess is that streamwise vortices driving the vibration in the pure cruciform case do not get initiated once

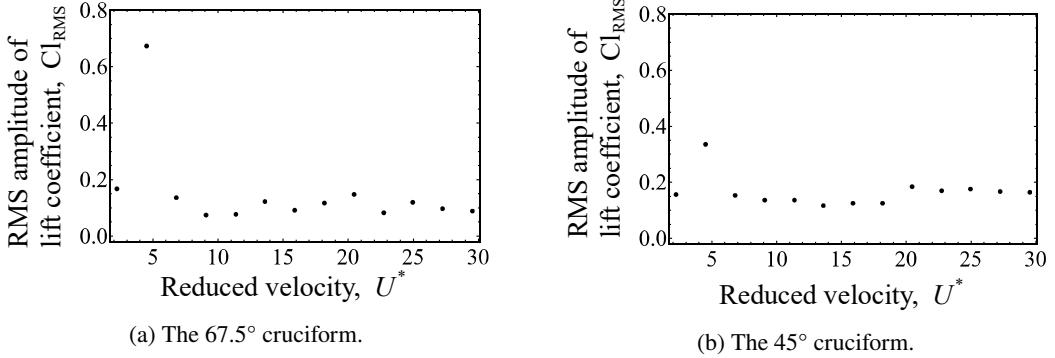


Figure 20: Evolution of the normalised Cl root-mean-square amplitude, Cl_{RMS} , with respect to reduced velocity U^* , for the 67.5° and 45° cruciforms.

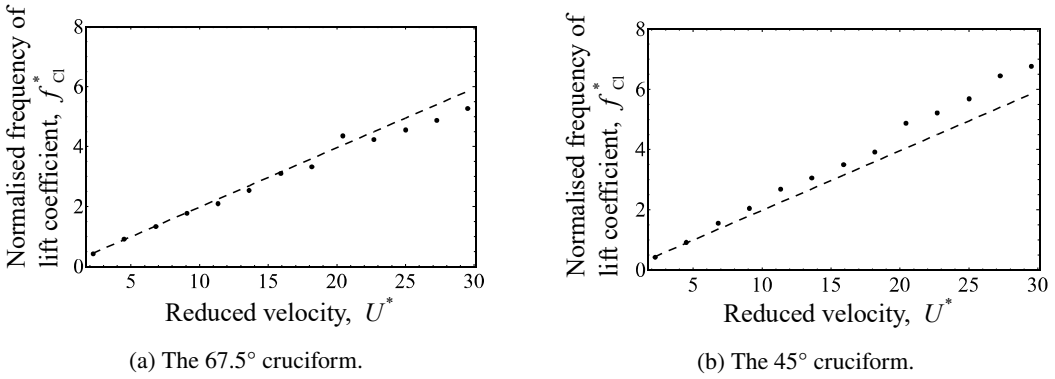


Figure 21: Evolution of the normalised Cl frequency, f_{CI}^* , with respect to reduced velocity U^* , for the 67.5° and 45° cruciforms. The dashed lines outline $f_{v,Karman}$ from Eq. 14.

the cruciform angle deviates away from 90° . However, x and z -component vorticity visualisations in Fig. 23 points out otherwise. These visualisations are produced under the same conditions as Fig. 16. Inspecting Figs. 23a and 23c, we can quite clearly make out the large-scale streamwise vortices close to the cruciform juncture. We thus expect the cylinder vibration and streamwise vortices to synchronise to each other, resulting in an $f^* \approx 1$ across the values of U^* after the lower branch of KVIV which appears at $U^* = 6.8$. In addition, we expect there to be a large amplitude response from the cylinder due to the formation and sustenance of the streamwise vortices close to the cruciform juncture. This was not the case.

We think the reason behind this lies in the distribution of the streamwise vortex cells along the cylinder axis. As we mentioned in §4.2, the streamwise vortex pair in the pure cruciform case lie on a plane parallel to the axis of the cylinder. The shared plane of formation parallel to cylinder axis is what we think as key to the large amplitude response observed in the pure cruciform case. A formation plane parallel to the cylinder axis ensures the resulting downward thrust to act perpendicular to the cylinder, securing a larger amplitude response. Also, the streamwise vortex cell on each side of the $Z = 0$ plane must be of opposing rotational direction for the production of thrust. We find these two

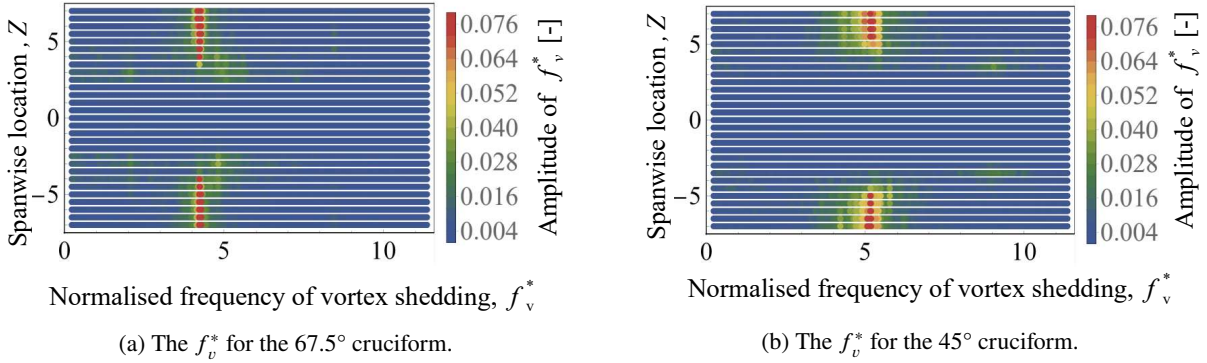


Figure 22: Distribution of normalised frequency of vortex shedding, along the span of the cylinder of the 67.5° and 45° cruciforms at $U^* = 22.7$.

aspects missing in the 67.5° and 45° cruciforms in Fig. 23.

What takes place in Figs. 23a and 23c is, two streamwise vortex cells of opposing poles form on each side of the $Z = 0$ plane. The result of this vortical arrangement is severe diminishing of useful thrust, and by extension, lift acting on the cylinder. This explains why the amplitude of f_v^* at and within the vicinity of 1 is extremely small in comparison to the dominant band close to $f_{v,\text{Karman}}^* = 4.49$, resulting in a low amplitude response for most of the U^* studied, even when $f^* \approx 1$.

We also managed to find the source of asymmetry in the vortical structure distribution around the cruciform, which becomes apparent upon closer comparison of Fig. 23b and Fig. 23d. The Karman vortices of the 67.5° cruciform are shed at different phases depending on which side of the $Z = 0$ plane we are observing. For the particular case in Fig. 23b, Karman vortices are being shed from the top of the cylinder when $Z < 0$, and from the bottom of the cylinder when $Z > 0$. What suggested this interpretation is our observation of a strong expression of $-z$ vorticity when $Z < 0$ from the top of the cylinder, while on the $Z > 0$ half of our domain is a strong expression of $+z$ vorticity from the bottom of the cylinder. We do not see this take place in Fig. 23d. On both sides of the $Z = 0$ plane, we note the strong expression of $-z$ vorticity from the top of the cylinder. This asymmetry leads to competing vibration-driving mechanisms resulting in the oscillatory behaviour of f^* seen in Fig. 19a.

5.3. Phase lag between Cl and y^*

Evolution of $\theta_{y-\text{Cl}}$ for the 67.5° and 45° cruciforms share a similar trend in the $2.3 \leq U^* \leq 6.8$ range. For the 67.5° cruciform, past $U^* = 6.8$, there seem to be two distinct VIV branches between $2.3 \leq U^* \leq 13.6$, and between $15.9 \leq U^* \leq 29.5$. In the first branch between $2.3 \leq U^* \leq 13.6$, $\theta_{y-\text{Cl}}$ seems to remain close to 70° , while in the second branch, close to 110° . In some sense, this is fairly similar to the $\theta_{y-\text{Cl}}$ vs. U^* pattern of the pure cruciform case, except for two features. First, the lower branch of KVIV – which in the pure cruciform case exhibits a $\theta_{y-\text{Cl}} \approx 180^\circ$ – does not extend beyond $U^* = 6.8$. Instead, the value for $\theta_{y-\text{Cl}}$ suddenly drops to $\approx 70^\circ$ before jumping back

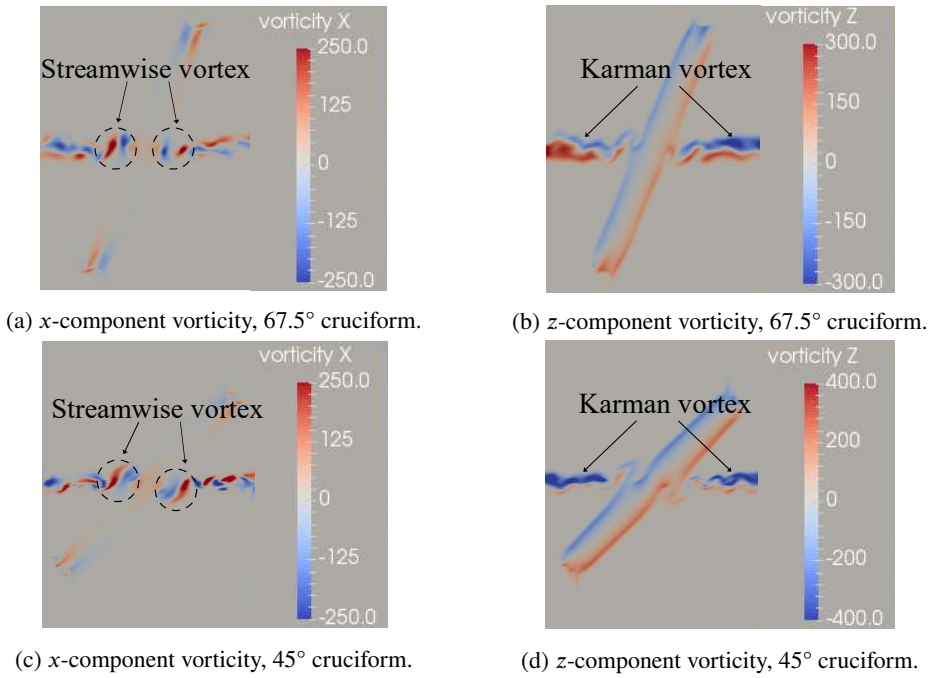


Figure 23: Dominant vortical structures at $U^* = 22.7$ observed in the 67.5° and 45° cases. The vorticity slices shown are the x and y -component vorticities (s^{-1}) at the $x/D = 1.96D$ plane, viewed orthogonal to that plane from downstream.

up to $\approx 110^\circ$ starting at $U^* = 15.9$. This value of 110° is curiously close to $\theta_{y-\text{Cl}}$ of the pure cruciform between $20.5 \leq U^* \leq 29.5$, equivalent to the upper branch of SVIV. If we work backwards from $U^* = 20.5$ in the direction of decreasing U^* , and compare Fig. 24a and Fig. 17, we confront the possibility that the $\theta_{y-\text{Cl}} = 70^\circ$ branch of the 67.5° cruciform is a *variant* of the SVIV initial branch. For the pure cruciform case, this occurs within a narrow window of $15.9 < U^* < 20.5$, with $\theta_{y-\text{Cl}} \approx 20^\circ$.

For the 45° cruciform in Fig. 24b, right after lower branch of KVIV at $U^* = 6.8$, $\theta_{y-\text{Cl}}$ transitioned to $\approx 65^\circ$ between $11.4 \leq U^* \leq 20.5$. The proximity between the values 65° and 70° for the 67.5° cruciform suggests the equivalence of the two branches. However, we are inclined to a more cautious conclusion: the two are *variants* of the same branch that is only similar in limited respects as they originate from different angled cruciforms. In this respect, the 45° cruciform is much less similar to the pure cruciform case, as one might expect, simply because 45° is a much larger deviation from 90° compared to 67.5° . This larger deviation is in our opinion what causes $\theta_{y-\text{Cl}}$ in the 45° case to drop further to $\approx 35^\circ$ within $22.7 \leq U^* \leq 29.5$, instead of jumping up to some mean value between $100 \leq \theta_{y-\text{Cl}} (\text{ }^\circ) \leq 130$ similar to what we observe in the 90° and 67.5° cruciforms.

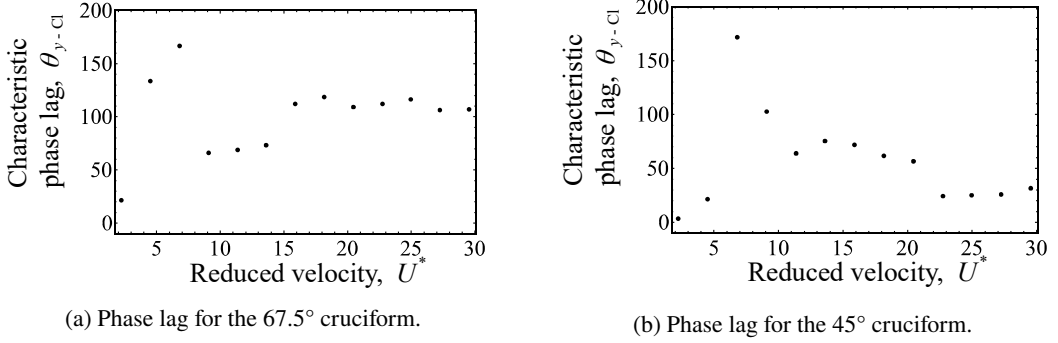


Figure 24: Phase lag $\theta_{y-\text{Cl}}$ ($^{\circ}$) between Cl and y^* when 67.5° and 45° .

6. Karman vortex-driven vibration

6.1. The amplitude and frequency response

As we decrease the cruciform angle even further to 22.5° , we observe a significant change in the amplitude and frequency response, compared to the transitional stage previously explored in §5. Consider Figs. 25a and 26a. There is no apparent KVIV upper branch similar to what we have seen in Figs. 18a and 19a at $U^* = 4.5$. Then, we observe no significant vibration elicited from the oscillator until $U^* = 20.5$. When $U^* = 20.5$, there is a abrupt jump in y_{RMS}^* from $y_{\text{RMS}}^* < 0.02$ to $y_{\text{RMS}}^* \approx 0.3$. The f^* vs. U^* trend demonstrated a bypassing of the KVIV lower branch - which occurred at $U^* = 6.8$ in the transitional stages of §5 - right into $f^* \approx 1$. Past $U^* = 20.5$, the value for y_{RMS}^* continues to increase and saturates at $U^* = 25.0$, and f^* continues to be close to 1 up to $U^* = 29.5$.

The 0° cruciform (Figs. 25b, 26b) in essence exhibits a very similar trend in its y_{RMS}^* and f^* evolutions with respect to U^* . However, the jump – which for the 22.5° cruciform occurs at $U^* = 20.5$ – occurs at a much lower $U^* = 9.1$. Then, y_{RMS}^* continues to grow until $U^* = 20.5$, reaching a staggering $y_{\text{RMS}}^* \approx 0.8$, a value no other study on energy harvesting using cruciform oscillators has ever achieved. The value of y_{RMS}^* then saturates close to 0.8 up to $U^* = 29.5$. Also similar to the 22.5° cruciform, f^* falls close to 1 at same U^* the y_{RMS}^* jump occurs - hinting at synchronisation between vortex shedding and system natural frequency.

Apart from the amplitude/frequency response of the 22.5° cruciform, the evolution of Cl_{RMS} against U^* showcases a similar trend to the evolution y_{RMS}^* , as shown in Fig. 27a. The corresponding f_{Cl}^* in Fig. 28a demonstrates the dominant frequency of Cl taking after Eq. 14 between $2.3 \leq U^* \leq 18.2$, before abruptly dropping close to 1 between $20.5 \leq U^* \leq 29.5$. This in part informs us that the flow between $2.3 \leq U^* \leq 18.2$ is governed by flow physics that are similar to both 67.5° and 45° within the same U^* range.

For the 0° cruciform, we see that the jump in Cl_{RMS} occurs at the same U^* as the jump in the corresponding y_{RMS}^* i.e., $U^* = 9.1$. After $U^* = 9.1$, the magnitude of Cl_{RMS} gradually drops to a final value of $\text{Cl}_{\text{RMS}} \approx 0.45$ at $U^* = 20.5$, and remains there up to $U^* = 29.5$. Similar to the 22.5° cruciform, f_{Cl}^* grows linearly in accordance with, again, Eq.

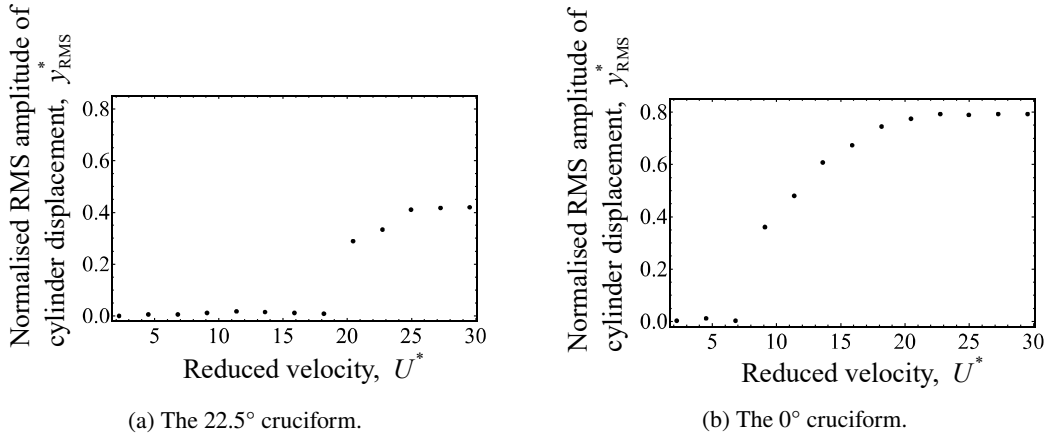


Figure 25: Evolution of the normalised root-mean-square amplitude of cylinder displacement y_{RMS}^* , with respect to reduced velocity U^* , for the 22.5° and 0° cruciform.

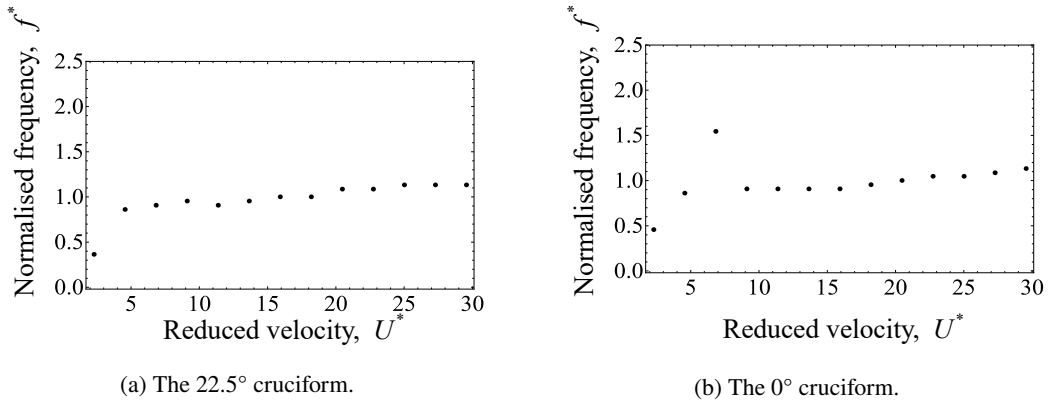


Figure 26: Evolution of the normalised cylinder displacement frequency, f^* , with respect to reduced velocity U^* , for the 22.5° and 0° cruciforms.

14 until the jump in both C_l^{RMS} and y_{RMS}^* , where $f_{C_l}^*$ drops close to 1 for the rest the U^* we examine in this study.

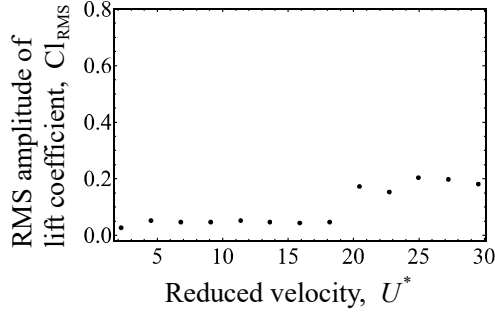
6.2. Main vibration-driving vortical structure

6.3. Phase lag between C_l and y^*

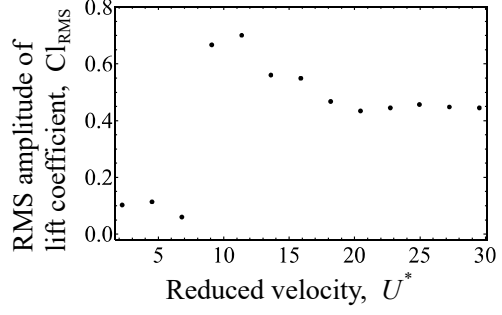
7. Power characteristic in $\alpha - U^*$ parameter space

8. Conclusions

In this study, we numerically investigated the temporal evolution of the lift coefficient and cylinder displacement signals of an elastically supported cruciform system in the range $1.1 \times 10^3 < \text{Re} < 14.6 \times 10^3$, or $2.3 < U^* < 29.5$. Our circular cylinder diameter is 10 mm and the natural frequency of the system is 4.4 Hz. Validation of key numerical results was made experimentally in a custom-built open flow channel, using a cruciform system whose parameters were tuned as close as possible to the quantities used in the numerical study. Decomposing the lift coefficient signal in

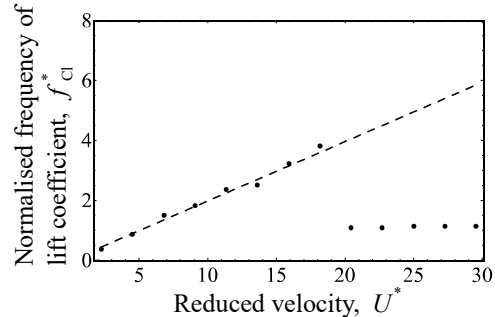


(a) The 22.5° cruciform.

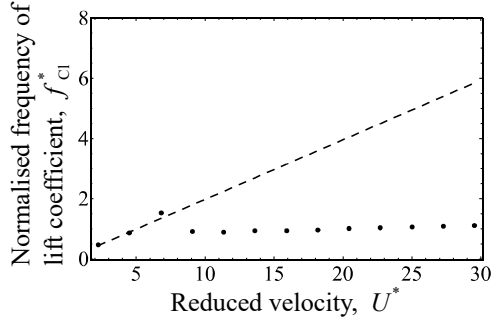


(b) The 0° cruciform.

Figure 27: Evolution of the normalised Cl root-mean-square amplitude, Cl_{RMS} , with respect to reduced velocity U^* , for the 22.5° and 0° cruciforms.



(a) The 22.5° cruciform.



(b) The 0° cruciform.

Figure 28: Evolution of the normalised Cl frequency, f_{Cl}^* , with respect to reduced velocity U^* , for the 22.5° and 0° cruciforms. The dashed lines outline $f_{v,Karman}$ from Eq. 14.

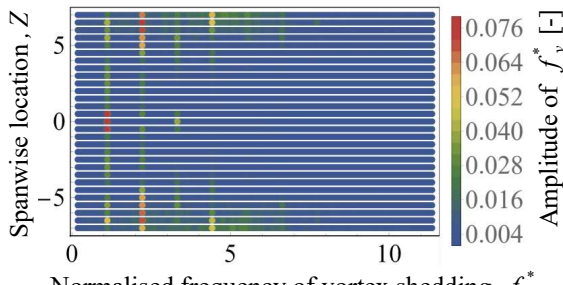
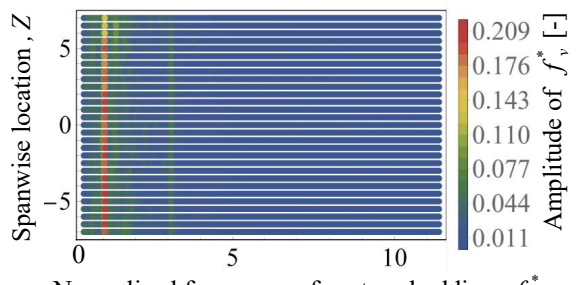
(a) The f_v^* for the 22.5° cruciform.(b) The f_v^* for the 0° cruciform.

Figure 29: Distribution of normalised frequency of vortex shedding, along the span of the cylinder of the 22.5° and 0° cruciforms at $U^* = 22.7$.

the SVIV regime ($15.9 \leq U^* \leq 29.5$) using EEMD allows us to see that the complexity of the lift coefficient signal as being caused by the superpositioning of two dominant components of lift. One due to the shedding of Karman and the other due to the shedding of streamwise vortices. The former has a frequency close to the vortex shedding frequency of Karman vortex from a smooth, isolated circular cylinder, while the latter has a mean frequency close to f_n . Application

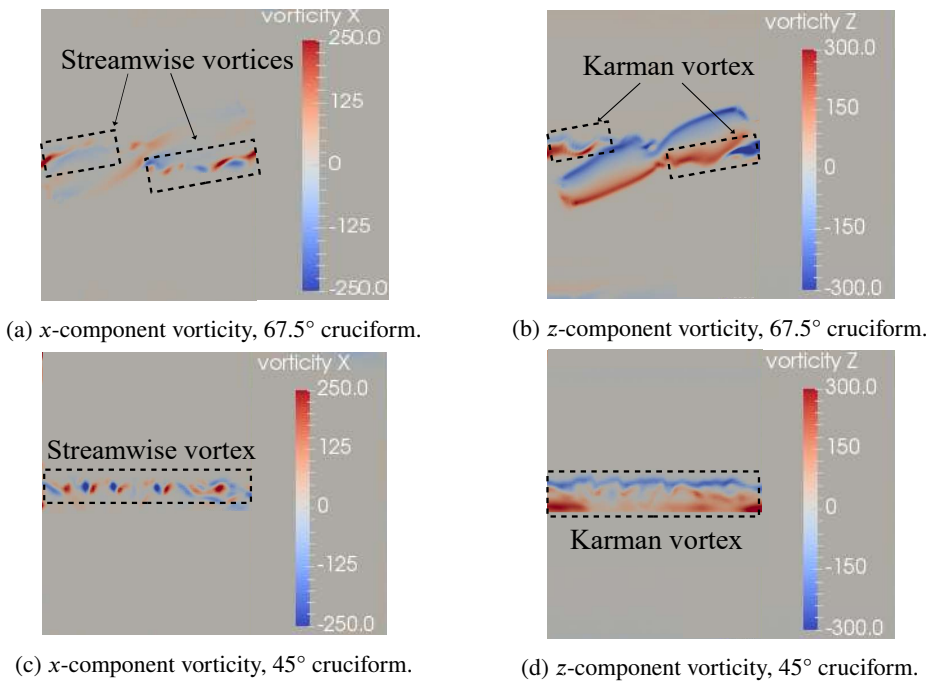


Figure 30: Dominant vortical structures at $U^* = 22.7$ observed in the 22.5° and 0° cases. The vorticity slices shown are the x and y -component vorticities (s^{-1}) at the $x/D = 1.96D$ plane, viewed orthogonal to that plane from downstream.

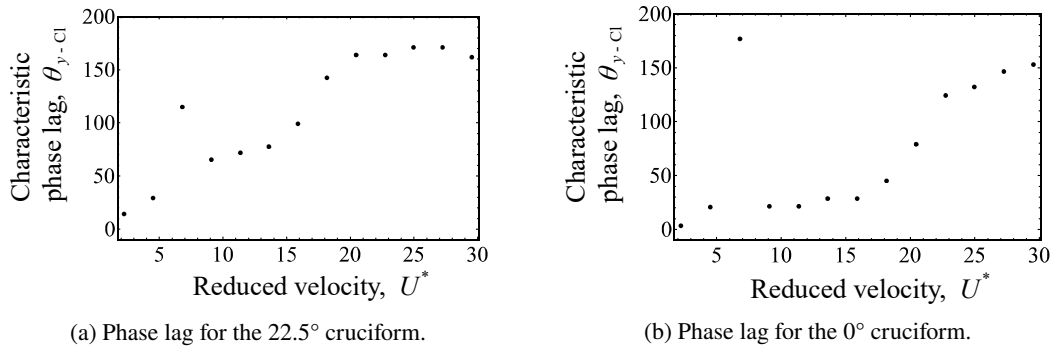


Figure 31: Phase lag θ_{y-Cl} ($^\circ$) between CL and y^* when 22.5° and 0° .

of the Hilbert-Huang transform on the dominant component of cylinder displacement – and the component of lift most correlated to it – allows for the computation of the instantaneous phase lag between lift and cylinder displacement. The time-averaged phase lag revealed five “branches” of vibration, among which is the initial branch of SVIV at $U^* = 18.2$, which has never been identified before in the literature. We also computed the instantaneous frequency of the lift coefficient, thus revealing the loss of periodicity and self-similarity in the lift coefficient signal as the system enters the SVIV regime. Estimation of power from our results show that the root-mean-square mechanical and fluid power computed from our experimental and numerical work agree to varying degrees depending on U^* with data from similar studies in the literature. Finally, we estimated that the root-mean-square fluid power can potentially be

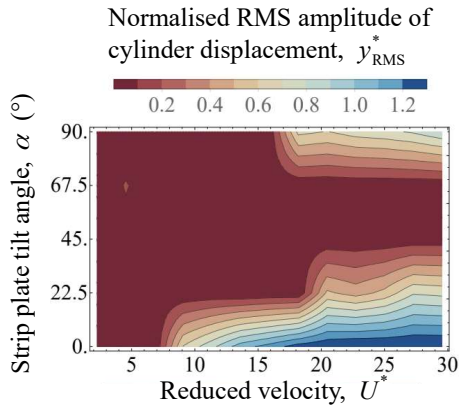


Figure 32: Isocontours describing the map of the normalised RMS amplitude of cylinder displacement, y_{RMS}^* in the cruciform angle - reduced velocity ($\alpha-U^*$) parameter space.

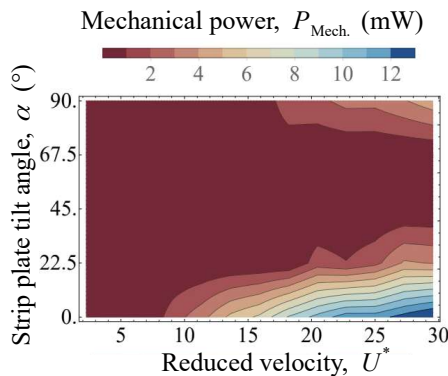


Figure 33: Isocontours describing the map of the estimated mechanical power in the cruciform angle - reduced velocity ($\alpha-U^*$) parameter space.

increased close to a factor of 2 within $18.2 \leq U^* \leq 22.7$ and close to a factor of 3 when $25.0 \leq U^* \leq 29.5$. We base this estimation on the premise of redirecting the contribution to the root-mean-square amplitude of total lift from Karman vortex shedding, towards the streamwise component of lift alone.

CRediT authorship contribution statement

Ahmad Adzlan: Conceptualisation, Methodology, Software, Validation, Formal analysis, Investigation, Data curation, Writing - Original draft preparation, Visualisation. **Mohamed Sukri Mat Ali:** Conceptualisation, Methodology, Resources, Writing - Review & Editing, Supervision, Project administration, Funding acquisition. **Sheikh Ahmad Zaki:** Resources, Writing - Review & Editing.

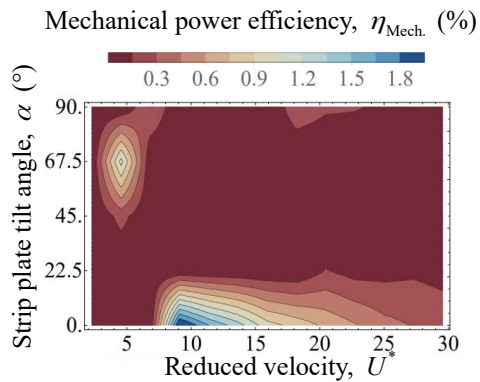


Figure 34: Isocontours describing the map of the estimated mechanical power in the cruciform angle - reduced velocity ($\alpha-U^*$) parameter space.

References

- Ali, M.S.M., Doolan, C.J., Wheatley, V., 2012. Low Reynolds number flow over a square cylinder with a detached flat plate. International Journal of Heat and Fluid Flow 36, 133–141. URL: <http://dx.doi.org/10.1016/j.ijheatfluidflow.2012.03.011>, doi:10.1016/j.ijheatfluidflow.2012.03.011.
- Bernitsas, M., Raghavan, K., 2008. Reduction/suppression of VIV of circular cylinders through roughness distribution at $8 \times 10^3 < \text{Re} < 1.5 \times 10^5$, in: Proceedings of the International Conference on Offshore Mechanics and Arctic Engineering - OMAE.
- Bernitsas, M.M., Ben-Simon, Y., Raghavan, K., Garcia, E.M.H., 2009. The VIVACE Converter: Model Tests at High Damping and Reynolds Number Around 10^5 . Journal of Offshore Mechanics and Arctic Engineering 131. URL: <http://offshoremechanics.asmedigitalcollection.asme.org/article.aspx?articleid=1472649>, doi:10.1115/1.2979796.
- Bernitsas, M.M., Raghavan, K., Ben-Simon, Y., Garcia, E.M.H., 2008. VIVACE (Vortex Induced Vibration Aquatic Clean Energy): A New Concept in Generation of Clean and Renewable Energy From Fluid Flow. Journal of Offshore Mechanics and Arctic Engineering 130, 041101. URL: <http://www.scopus.com/record/display.url?eid=2-s2.0-56749179917&origin=resultslist&sort=plf-f&src=s&st1=A+new+concept+in+generation+of+clean+and+renewable+energy+from+fluid+flow&sid=620865A71FAF26768C42655E1E8BC194.aXczxbyuHHiXgaIW6Ho7g:230&sot=b&sdt=b&h>, doi:10.1115/1.2957913.
- Blevins, R.D., 1990. Flow-induced vibration .
- Deng, J., Ren, A.L., Shao, X.M., 2007. The flow between a stationary cylinder and a downstream elastic cylinder in cruciform arrangement. Journal of Fluids and Structures 23, 715–731. URL: <https://www.sciencedirect.com/science/article/pii/S0889974606001472>, doi:10.1016/J.JFLUIDSTRUCTS.2006.11.005.
- Ding, L., Zhang, L., Kim, E.S., Bernitsas, M.M., 2015a. URANS vs. experiments of flow induced motions of multiple circular cylinders with passive turbulence control. Journal of Fluids and Structures 54, 612–628. doi:10.1016/j.jfluidstructs.2015.01.003.
- Ding, L., Zhang, L., Wu, C., Mao, X., Jiang, D., 2015b. Flow induced motion and energy harvesting of bluff bodies with different cross sections. Energy Conversion and Management doi:10.1016/j.enconman.2014.12.039.
- Ding, W., Sun, H., Xu, W., Bernitsas, M.M., 2019. Numerical investigation on interactive FIO of two-tandem cylinders for hydrokinetic energy harnessing. Ocean Engineering 187, 106215. URL: <https://www.sciencedirect.com/science/article/pii/S0029801819304019>, doi:10.1016/J.OCEANENG.2019.106215.
- Duranay, A., Kinaci, O.K., 2020. Enhancing two-dimensional computational approach for vortex-induced vibrations by scaling lift force. Ocean

Energy Harvesting from an Angled Cruciform

Engineering 217, 107620. doi:10.1016/j.oceaneng.2020.107620.

Feng, C.C., 1963. The measurement of vortex induced effects in flow past stationary and oscillating circular and D-section cylinders , 100.

Hemsuwan, W., Sakamoto, K., Takahashi, T., 2018a. Lift Force Generation of a Moving Circular Cylinder with a Strip-Plate Set Downstream in Cruciform Arrangement: Flow Field Improving Using Tip Ends. International Journal of Aeronautical and Space Sciences 19, 606–617. URL: <http://link.springer.com/10.1007/s42405-018-0068-5>, doi:10.1007/s42405-018-0068-5.

Hemsuwan, W., Sakamoto, K., Takahashi, T., 2018b. Numerical investigation of lift-force generation on a moving circular cylinder in a uniform flow driven by longitudinal vortex. Journal of Fluids and Structures 83, 448–470. URL: <https://www.sciencedirect.com/science/article/pii/S0889974617308885>, doi:10.1016/J.JFLUIDSTRUCTS.2018.09.010.

Huang, N.E., 2014. Hilbert-Huang transform and its applications. volume 16. World Scientific.

Huang, N.E., Attoh-Okine, N.O., 2005. The Hilbert-Huang transform in engineering. CRC Press.

Huang, N.E., Shen, Z., Long, S.R., Wu, M.C., Srinivasa, H.H., Zheng, Q., Yen, N.C., Tung, C.C., Liu, H.H., 1998. The empirical mode decomposition and the Hilbert spectrum for nonlinear and non-stationary time series analysis. Proceedings of the Royal Society A: Mathematical, Physical and Engineering Sciences doi:10.1098/rspa.1998.0193.

Kawabata, Y., Takahashi, T., Hagiwara, T., Shirakashi, M., 2013. Interference Effect of Downstream Strip-Plate on the Crossflow Vibration of a Square Cylinder. Journal of Fluid Science and Technology 8, 647–658. doi:10.1299/jfst.8.348.

Khalak, A., Williamson, C., 1999. Motions, Forces And Mode Transitions In Vortex-Induced Vibrations At Low Mass-Damping. Journal of Fluids and Structures 13, 813–851. URL: <http://www.sciencedirect.com/science/article/pii/S0889974699902360>, doi:10.1006/jfls.1999.0236.

Kinaci, O.K., Lakka, S., Sun, H., Bernitsas, M.M., 2016. Effect of tip-flow on vortex induced vibration of circular cylinders for Re. Ocean Engineering 117, 130–142. URL: <http://www.sciencedirect.com/science/article/pii/S002980181630018X>, doi:10.1016/j.oceaneng.2016.03.055.

Koide, M., Kato, N., Yamada, S., Kawabata, Y., Takahashi, T., Shirakashi, M., 2007. Influence Of A Cruciform Arrangement Downstream Strip-Plate On Crossflow Vibration. Journal of Computational and Applied Mechanics 8, 135–148.

Koide, M., Ootani, K., Yamada, S., Takahashi, T., Shirakashi, M., 2006. Vortex Excitation Caused by Longitudinal Vortices Shedding from Cruciform Cylinder System in Water Flow. JSME International Journal 49, 1043–1048.

Koide, M., Sekizaki, T., Yamada, S., Takahashi, T., Shirakashi, M., 2009. A Novel Technique for Hydroelectricity Utilizing Vortex Induced Vibration, in: Proceedings of the ASME Pressure Vessels and Piping Division Conference, PVP2009-77487.

Koide, M., Sekizaki, T., Yamada, S., Takahashi, T., Shirakashi, M., 2013. Prospect of Micro Power Generation Utilizing VIV in Small Stream Based on Verification Experiments of Power Generation in Water Tunnel. Journal of Fluid Science and Technology 8, 294–308. URL: https://www.jstage.jst.go.jp/article/jfst/8/3/8f_294/_article <http://jlc.jst.go.jp/DN/JST.JSTAGE/jfst/8.294?lang=en&from=CrossRef&type=abstract>, doi:10.1299/jfst.8.294.

Koide, M., Takahashi, T., Shirakashi, M., Salim, S.A.Z.B.S., 2017. Three-dimensional structure of longitudinal vortices shedding from cruciform two-cylinder systems with different geometries. Journal of Visualization , 1–11.

Krishnendu, P., Ramakrishnan, B., 2020. Performance analysis of dual sphere wave energy converter integrated with a chambered breakwater system. Applied Ocean Research 101, 102279. doi:10.1016/j.apor.2020.102279.

Langley Research Centre, 2018. Turbulence Modeling Resource. URL: <https://turbmodels.larc.nasa.gov/>.

Maruai, N.M., Ali, M.S.M., Ismail, M.H., Zaki, S.A., 2018. Flow-induced vibration of a square cylinder and downstream flat plate associated with micro-scale energy harvester. Journal of Wind Engineering and Industrial Aerodynamics 175, 264–

Energy Harvesting from an Angled Cruciform

282. URL: <https://www.scopus.com/inward/record.uri?eid=2-s2.0-85042219159&doi=10.1016%2Fj.jweia.2018.01.010&partnerID=40&md5=2f3f62b94bb69ced3368b32e682aefc7>, doi:10.1016/j.jweia.2018.01.010.
- Maruai, N.M., Mat Ali, M.S., Ismail, M.H., Shaikh Salim, S.A.Z., 2017. Downstream flat plate as the flow-induced vibration enhancer for energy harvesting. *Journal of Vibration and Control* , 107754631770787URL: <http://journals.sagepub.com/doi/10.1177/1077546317707877>, doi:10.1177/1077546317707877.
- Mat Ali, M.S., Doolan, C.J., Wheatley, V., 2011. Low Reynolds number flow over a square cylinder with a splitter plate. *Physics of Fluids* 23. doi:10.1063/1.3563619.
- Nguyen, T., Koide, M., Yamada, S., Takahashi, T., Shirakashi, M., 2012. Influence of mass and damping ratios on VIVs of a cylinder with a downstream counterpart in cruciform arrangement. *Journal of Fluids and Structures* 28, 40–55. doi:10.1016/j.jfluidstructs.2011.10.006.
- Richardson, L.F., Gaunt, J.A., 1927. The deferred approach to the limit. *Philosophical Transactions of the Royal Society A* doi:<https://doi.org/10.1098/rsta.1927.0008>.
- Shirakashi, M., Mizuguchi, K., Bae, H.M., 1989. Flow-induced excitation of an elastically-supported cylinder caused by another located downstream in cruciform arrangement. *Journal of Fluids and Structures* 3, 595–607. doi:10.1016/S0889-9746(89)90150-3.
- Spalart, P., Allmaras, S., 1992. A one-equation turbulence model for aerodynamic flows, in: 30th Aerospace Sciences Meeting and Exhibit. URL: <http://arc.aiaa.org/doi/10.2514/6.1992-439>, doi:10.2514/6.1992-439, arXiv:arXiv:1011.1669v3.
- Stern, F., Wilson, R.V., Coleman, H.W., Paterson, E.G., 2001. Comprehensive approach to verification and validation of CFD simulations; part I: methodology and procedures. *Journal of fluids engineering* 123, 793–802.
- Sun, H., Kim, E.S., Nowakowski, G., Mauer, E., Bernitsas, M.M., 2016. Effect of mass-ratio, damping, and stiffness on optimal hydrokinetic energy conversion of a single, rough cylinder in flow induced motions. *Renewable Energy* 99, 936–959. URL: <http://www.sciencedirect.com/science/article/pii/S0960148116306206>, doi:10.1016/j.renene.2016.07.024.
- Sun, H., Ma, C., Kim, E.S., Nowakowski, G., Mauer, E., Bernitsas, M.M., 2019. Flow-induced vibration of tandem circular cylinders with selective roughness: Effect of spacing, damping and stiffness. *European Journal of Mechanics, B/Fluids* 74, 219–241. doi:10.1016/j.euromechflu.2018.10.024.
- Wen, C., Wang, J., Zhang, Y., Xu, T., Zhang, X., Ning, Y., 2020. Vehicle Trajectory Clustering and Anomaly Detection at Freeway Off-Ramp Based on Driving Behavior Similarity, in: CICTP 2020, American Society of Civil Engineers, Reston, VA. pp. 4220–4232. URL: <http://ascelibrary.org/doi/10.1061/9780784482933.362>, doi:10.1061/9780784482933.362.
- Wu, Z., Huang, N.E., 2008. Ensemble Empirical Mode Decomposition: A Noise-Assisted Data Analysis Method. *Advances in Adaptive Data Analysis* doi:10.1142/s1793536909000047.
- Zhang, B., Mao, Z., Song, B., Ding, W., Tian, W., 2018. Numerical investigation on effect of damping-ratio and mass-ratio on energy harnessing of a square cylinder in FIM. *Energy* 144, 218–231. URL: <https://www.scopus.com/inward/record.uri?eid=2-s2.0-85037995662&doi=10.1016%2Fj.energy.2017.11.153&partnerID=40&md5=01db7c6b6d4d44e88de7045843c7d423>, doi:10.1016/j.energy.2017.11.153.
- Zhao, M., Lu, L., 2018. Numerical simulation of flow past two circular cylinders in cruciform arrangement. *Journal of Fluid Mechanics* 848, 1013–1039. URL: https://www.cambridge.org/core/product/identifier/S0022112018003804/type/journal_article, doi:10.1017/jfm.2018.380.